Multiscale Modeling of Point and Line Defects in Cubic Lattices

by P. W. Chung and J. D. Clayton

ARL-RP-200   **March 2008**

NOTICES

Disclaimers

Army Research Laboratory
Aberdeen Proving Ground, MD 21005-5069

Multiscale Modeling of Point and Line Defects in Cubic Lattices

P. W. Chung and J. D. Clayton
Weapons and Materials Research Directorate, ARL

REPORT DOCUMENTATION PAGE

Form Approved
OMB No. 0704-0188

1. REPORT DATE *(DD-MM-YYYY)*	2. REPORT TYPE	3. DATES COVERED *(From - To)*
March 2008	Reprint	January 2005–January 2007

4. TITLE AND SUBTITLE	5a. CONTRACT NUMBER
Multiscale Modeling of Point and Line Defects in Cubic Lattices	
	5b. GRANT NUMBER
	5c. PROGRAM ELEMENT NUMBER
6. AUTHOR(S)	**5d. PROJECT NUMBER**
P. W. Chung and J. D. Clayton	DRI-FY05-CIS10
	5e. TASK NUMBER
	5f. WORK UNIT NUMBER

7. PERFORMING ORGANIZATION NAME(S) AND ADDRESS(ES)	8. PERFORMING ORGANIZATION REPORT NUMBER
U.S. Army Research Laboratory ATTN: AMSRD-ARL-WM-TD Aberdeen Proving Ground, MD 21005-5069	ARL-RP-200

9. SPONSORING/MONITORING AGENCY NAME(S) AND ADDRESS(ES)	10. SPONSOR/MONITOR'S ACRONYM(S)
	11. SPONSOR/MONITOR'S REPORT NUMBER(S)

12. DISTRIBUTION/AVAILABILITY STATEMENT

Approved for public release; distribution is unlimited.

13. SUPPLEMENTARY NOTES

14. ABSTRACT

A multilength scale method based on asymptotic expansion homogenization (AEH) is developed to compute minimum energy configurations of ensembles of atoms at the fine length scale and the corresponding mechanical response of the material at the coarse length scale. This multiscale theory explicitly captures heterogeneity in microscopic atomic motion in crystalline materials, attributed, for example, to the presence of various point and line lattice defects. The formulation accounts for large deformations of nominally hyperelastic, monocrystalline solids. Unit cell calculations are performed to determine minimum energy configurations of ensembles of atoms of body-centered cubic tungsten in the presence of periodic arrays of vacancies and screw dislocations of line orientations [111] or [100]. Results of the theory and numerical implementation are verified versus molecular statics calculations based on conjugate gradient minimization (CGM) and are also compared with predictions from the local Cauchy-Born rule. For vacancy defects, the AEH method predicts the lowest system energy among the three methods, while computed energies are comparable between AEH and CGM for screw dislocations. Computed strain energies and defect energies (e.g., energies arising from local internal stresses and strains near defects) are used to construct and evaluate continuum energy functions for defective crystals parameterized via the vacancy density, the dislocation density tensor, and the generally incompatible lattice deformation gradient. For crystals with vacancies, a defect energy increasing linearly with vacancy density and applied elastic deformation is suggested, while for crystals with screw dislocations, a defect energy linearly dependent on the dislocation density tensor appears more appropriate than the quadratic dependency often encountered in the continuum plasticity literature.

15. SUBJECT TERMS

multiscale, atomistic, elasticity, dislocations, vacancies, homogenization

16. SECURITY CLASSIFICATION OF:			17. LIMITATION OF ABSTRACT	18. NUMBER OF PAGES	19a. NAME OF RESPONSIBLE PERSON Peter W. Chung
a. REPORT UNCLASSIFIED	**b. ABSTRACT** UNCLASSIFIED	**c. THIS PAGE** UNCLASSIFIED	UL	30	19b. TELEPHONE NUMBER *(Include area code)* 410-306-0975

Standard Form 298 (Rev. 8/98)
Prescribed by ANSI Std. Z39.18

Multiscale Modeling of Point and Line Defects in Cubic Lattices

P. W. Chung & J. D. Clayton

U.S. Army Research Laboratory, Aberdeen Proving Ground, MD 21005, USA

ABSTRACT

A multilength scale method based on asymptotic expansion homogenization (AEH) is developed to compute minimum energy configurations of ensembles of atoms at the fine length scale and the corresponding mechanical response of the material at the coarse length scale. This multiscale theory explicitly captures heterogeneity in microscopic atomic motion in crystalline materials, attributed, for example, to the presence of various point and line lattice defects. The formulation accounts for large deformations of nominally hyperelastic, monocrystalline solids. Unit cell calculations are performed to determine minimum energy configurations of ensembles of atoms of body-centered cubic tungsten in the presence of periodic arrays of vacancies and screw dislocations of line orientations [111] or [100]. Results of the theory and numerical implementation are verified versus molecular statics calculations based on conjugate gradient minimization (CGM) and are also compared with predictions from the local Cauchy-Born rule. For vacancy defects, the AEH method predicts the lowest system energy among the three methods, while computed energies are comparable between AEH and CGM for screw dislocations. Computed strain energies and defect energies (e.g., energies arising from local internal stresses and strains near defects) are used to construct and evaluate continuum energy functions for defective crystals parameterized via the vacancy density, the dislocation density tensor, and the generally incompatible lattice deformation gradient. For crystals with vacancies, a defect energy increasing linearly with vacancy density and applied elastic deformation is suggested, while for crystals with screw dislocations, a defect energy linearly dependent on the dislocation density tensor appears more appropriate than the quadratic dependency often encountered in the continuum plasticity literature.

*Address all correspondence to jclayton@arl.army.mil

1. INTRODUCTION

Multiscale methods often establish constraints that permit numerical juxtaposition of discrete and continuum material descriptions. This necessarily requires enforcement of kinematic approximations to enforce compatibility between two otherwise disparate domains to reduce the overall number of degrees of freedom and produce a computationally tractable problem. One such kinematic approximation is the Cauchy-Born rule (CB), which enforces tangent maps at the fine scale to simulate the locally homogeneous deformation of bulk three-dimensional crystals [1,2]. Detailed expositions of the underlying theory can be found in several references [3–5]. The utility of the CB is not confined exclusively to bulk crystals. Following extension of the Cartesian theory commonly used for bulk lattices to curvilinear manifolds, deformations of planar and lower dimensional monocrystals can be efficiently described as well [6–8].

The importance of these types of kinematic approximations manifests in their continued foundational presence in multiscale methods for materials modeling. Early models used to study atomistic processes in the vicinity of crack tips or dislocation cores relied heavily on continuum elasticity theory, without including atoms in the far-field. Early work featured one-way [9–14] or two-way [15–19] coupled methods, in which displacement fields established at the interface between continuum and atomistic regions were computed either from sophisticated interfacial conditions or from initial conditions derived from continuum elasticity theory. Increases in computing power permitted more realistic two-way couplings, whereby atomistic fields were permitted to affect the far-field elastic continua through the latter's discretization with finite elements [20–23]. Such improvements in the coupling algorithms enabled description of dynamic crack growth [21]. These approximations were also prudent at the time as uninteresting effects in nearly homogeneously deforming regions far from defects could be disregarded and because of the limitations of then available computing resources.

Novel methods involving electronic structure have permitted consideration of higher accuracy calculations in the near field [24,25], with the finite element domain in the far-field remaining essentially linear elastic. Although some early work attempted to parameterize stress-strain relationships in the far-field region with atomic potentials [20–22], more efficient considerations of selected atomistic effects on material behavior were achieved through the initial developments of the quasicontinuum theory [26–28] that employed hyperelastic constitutive behavior, derived from atomistic potentials, for the overlaying finite elements. In the subsequent decade, significant new developments in methodologies have improved the fidelity of atomistically informed, continuum multiscale computational methods [29–31].

The multiscale modeling approaches discussed thus far reduce the problem dimensionality through various kinematic approximations such as the CB. Even with presumable improvements in the performance of future generations of microprocessors, the increasing demand of higher-fidelity modeling [32] will require increases in computational resources that will outpace projected computer hardware improvements. Such demands in fidelity mandate improvements over the CB in situations involving, for example, large defect densities [33] and complex active lattices [34].

Tewary and colleagues [35,36] demonstrated the feasibility of representing lattice defects in reduced form using Green's function methods. In such a lower-order method, the defect core can be represented with semianalytical functions, thereby providing an initial estimate that can be used as an initial state in a more computationally intensive, larger-scale atomistic simulation. However, general situations involving heterogeneous strain fields and high defect densities, as opposed to isolated defects, are usually not considered. Furthermore, increasing evidence supports the idea that concurrent simulations at finite temperature in which a statistical (quantum mechanical) or discrete (molecular) domain is interfaced with a continuum domain presents profound obstacles to computer method development [37–40]. Although the present investigation is restricted to quasi-static isothermal conditions, it is noteworthy that self-consistent hierarchical approaches provide a means of preserving statistical ensembles of atomic motions in the continuum domain, such as at a finite element quadrature point, through the use of unit cell-based averaging.

The asymptotic expansion homogenization (AEH) method is formulated and implemented in the present article, building on the original

theory of Chung and colleagues [41,42]. Discrete simulations are executed at the atomistic level, with each volume element (unit cell) of atoms subjected to periodic boundary conditions. Asymptotic homogenization methods [43,44] are used to compute the macroscopic tangent stiffness associated with the mechanical response of the ensemble of atoms in the unit cell. The CB kinematic rule is invoked for imposition of the bulk continuum deformation, with the fine-scale displacements of individual atoms identified with the inner displacements in the asymptotic approximation. The present approach appears ideal in its present form for addressing the response of microstructures containing periodically distributed defects, in contrast to other methods (e.g., [26]) initially developed to address isolated defects. This is because only one or a few defects need be simulated explicitly at the atomistic level within the context of the periodicity assumption invoked in our homogenization scheme. However, owing to this very same periodicity assumption, the method suffers in the sense that isolated (i.e., nonrepeating) defects cannot be easily modeled. Specifically, previous applications of AEH involved modeling the elastic response of graphene with point defects [41,42] and incorporation of the kinematics and energetics of finite plastic deformation in metallic crystals at the coarse scale [45]. Other developments have appeared in the generalized mathematical homogenization method [46,47] to more carefully account for the dynamical and thermal behavior of atoms.

Noteworthy developments discussed in the present article include simulations, in deforming metallic crystals, of vacancies and of dislocations of orientations not considered previously [45] as well as parameterization and comparison of energy density functions from continuum defect field (CDF) theory with those computed using the AEH method. Regarding the first development, the AEH method is demonstrated to predict atomic configurations of unit cells containing defects with nearly equal, and in some cases lower, system energies than conventional lattice statics methods [48,49] based on conjugate gradient minimization (CGM). Comparison with results from CGM is of interest because CGM is often invoked at the fine scale in other popular multiscale methods such as the quasicontinuum theory [26–28]. For the defects considered here, both AEH and CGM are shown to predict

more realistic, lower-energy atomic configurations than the local CB rule.

Regarding the second development, some background discussion on continuum field theories of defects is now warranted. As described here, these constitute a class of elastic-plastic material models for crystalline solids that are also multiscale theories, though discrete atoms are not involved at the fine scale. Rather, effects of defects and other sources of microstructural heterogeneity are reflected in the material response functions (e.g., stored energy, yield stress, or hardening parameters) through kinematic variables, internal state variables, and spatial gradients of these variables [50–55]. Such representations account for strain hardening in plasticity of single crystals [52,53]; evolution of microstructures associated with point, line, and surface defects [54,55]; and regularization of numerical instabilities in continuum inelasticity implementations [56,57].

While nonlinear elastic moduli for defect-free crystals have been parameterized versus deformation [58,59], continuum-level energy functions of materials with periodically distributed defects such as vacancies and dislocations have heretofore not been explicitly parameterized, simultaneously, versus defect density and applied deformation using atomistic modeling tools. In many cases, simple phenomenological formulations are used for defect-dependent strain energy in continuum material models. These formulations may either be motivated from microscopic physics, or may be used simply because energetic data are unavailable. For porous materials (i.e., those with vacancy defects), the elastic strain energy is typically reduced linearly with vacancy concentration such that stress is linearly reduced [60] along the lines of isotropic damage mechanics theory [61]. For dislocations, energy functions, either linear or quadratic, in the line density of dislocations per unit area have been assumed. In strain gradient–based continuum dislocation theories, dislocation populations are often partitioned into statistically stored dislocation (SSD) and geometrically necessary dislocation (GND) families, following [62]. The former include closed dislocation loops and contribute no net Burgers vector, while the latter are a measure of the incompatibility of the elastic (or plastic) deformation field. Typically, a linear dependence of stored (or free) energy of the crystalline material on SSDs or total disloca-

tion density [63] is assumed. On the other hand, quadratic functions are often used to account for the local strain energy imparted by the GND tensor [51–53,55]. This form is used for simplicity, motivated by analogy to linear elasticity theory, and also is used to provide a back stress dependent on the density of dislocations [60,64] or its gradient [51,53]. Remaining open issues pertaining to continuum modeling of dislocation defects in the context of gradient plasticity are quantification of the length scale parameter(s) required to normalize the energy [65] and proper selection of the metric tensor used to collapse the GND tensor to scalar form [55,66].

In the present work, numerical results obtained from execution of the AEH multiscale method are used to motivate the choice of continuum energy functions and associated parameters, in particular for single crystalline tungsten (W) containing vacancies or screw dislocations. Only energies are considered, and not stresses, in part because the latter are not trivially defined from an atomistic perspective [67]. The investigation is limited in the sense that only a few classes of defects are examined, for only one material (W), and these defects are arranged periodically in the lattice. Furthermore, all simulations are isothermal at null temperature (akin to molecular statics). However, this work constitutes an initial step toward computing energies used in continuum defect theories from physics-based, multiscale computations, as opposed to phenomenological curve fitting of the material response to macroscopic stress data, for example. Intermediate scale methods, such as phase field models [68,69] or discrete dislocation simulations [70–72], may ultimately be needed to address nonideal defect configurations and finite temperature defect kinetics to bridge scales of atomistic resolution and continuum crystal mechanics for arbitrarily disordered states of the material.

The remainder of this article is organized as follows. Section 2 features derivations of the multiscale homogenization equations applicable to geometrically nonlinear problems, with discrete atoms resolved at the fine scale. Section 3 includes discussion of numerical implementation and specialization of the theory to tungsten crystals. Results of demonstrative simulations of defects in the atomistic domain are given in Section 4. These results are applied toward development of continuum-scale defect field descriptions in Section 5. Vectors and tensors are written in boldface type, with scalars and individual components of vectors and tensors written in italic font. The indicial notation is frequently employed, with summation implied over repeated indices, for example, $A^a B_a = A^1 B_1 + A^2 B_2 + A^3 B_3$ when $a = 1, 2, 3$.

2. THEORY

Reference and current configurations of a continuous body, denoted by B_0 and B, respectively, are introduced. Let $\mathbf{X}$ and $\mathbf{x}$ denote coordinates spanning the reference and spatial frames, and let $x^a = x^a(X^A, t)$ denote the differentiable motion of the material, with t denoting time. The deformation gradient or tangent mapping $\mathbf{F}$ from B_0 to B is then written as

$$\mathbf{F} = \frac{\partial \mathbf{x}}{\partial \mathbf{X}} \quad F^a_{.A} = \frac{\partial x^a}{\partial X^A} \tag{1}$$

Strain measures are introduced as follows, where $G_{AB} = \partial_A \mathbf{X} \cdot \partial_B \mathbf{X}$ and $g_{ab} = \partial_a \mathbf{x} \cdot \partial_b \mathbf{x}$ are, respectively, metric tensors in reference and spatial coordinate systems:

$$C_{AB} = F^a_{.A} g_{ab} F^b_{.B} \quad 2E_{AB} = F^a_{.A} g_{ab} F^b_{.B} - G_{AB} \tag{2}$$

Denoted by $\boldsymbol{\Sigma}$, $\mathbf{P}$, and $\mathbf{S}$, the Cauchy stress, first Piola-Kirchhoff stress, and second Piola-Kirchhoff stress, respectively, are related by

$$\Sigma^{ab} = J^{-1} F^a_{.A} P^{bA} = J^{-1} F^a_{.A} S^{AB} F^b_{.B} \tag{3}$$

Assuming quasi-static conditions, local forms of the balances of linear and angular momentum are written as follows:

$$P^{aA}_{|A} + B^a = 0 \quad F^a_{.A} P^{bA} = P^{aA} F^b_{.A} \tag{4}$$

where the vertical bar denotes covariant differentiation and $\mathbf{B}$ is the body force vector per unit reference volume. The usual symmetry relations for stress tensors hold from Eq. (3) and the second of Eq. (4), $\Sigma^{ab} = \Sigma^{(ab)}$ and $S^{AB} = S^{(AB)}$, where parentheses indicate symmetrization, that is, $2A^{(ab)} = A^{ab} + A^{ba}$ for arbitrary second-rank tensor $\mathbf{A}$. Multiplying the first of Eq. (4) by virtual displacement $\delta \mathbf{u}$ and integrating over reference volume V, the following virtual work principle is obtained:

$$\int_V P^{aB} g_{ab} \left(\delta u\right)^b_{|B} dV = \int_{\partial V} T^a g_{ab} \delta u^b dA$$
$$+ \int_V B^a g_{ab} \delta u^b dV \tag{5}$$

with the traction per unit reference area A given by $T^a = P^{aB} N_B$, where N_B are covariant components of the unit normal vector to external boundary ∂V. Here a free energy potential Ψ per unit reference volume on B_0 is assumed to exist, with the stress tensor satisfying the following hyperelastic relationships:

$$S^{AB} = 2\frac{\partial \Psi}{\partial C_{AB}} = \frac{\partial \Psi}{\partial E_{AB}} \tag{6}$$

For the particular case of first-order hyperelasticity, Eq. (6) becomes

$$S^{AB} = \frac{\partial^2 \Psi}{\partial E_{AB} \partial E_{CD}} E_{CD} = \mathbb{C}^{ABCD} E_{CD} \tag{7}$$

where $\mathbb{C}^{ABCD} = \mathbb{C}^{(AB)(CD)}$ is the fourth-rank tensor of elastic moduli in the reference frame. Substituting Eq. (6) into Eq. (5) and using Eq. (3),

$$\int\limits_V 2F^a_{.A} \frac{\partial \Psi}{\partial C_{AB}} g_{ab} \left(\delta u\right)^b_{|B} \, dV = \int\limits_{\partial V} T^a g_{ab} \delta u^b dA$$

$$+ \int\limits_V B^a g_{ab} \delta u^b dV \tag{8}$$

The link between atomistic (fine scale) and continuum (coarse scale) resolutions is established here via the AEH technique [41,42,45]. Let fine and coarse length scales be spanned by coordinates $y^a = y^a(Y^A, t)$ and $x^a = x^a(X^A, t)$, respectively. Although multiple time scales have been used elsewhere [73], in the present scheme, both scales are parameterized by the same temporal variable t. Multiscale coordinates are related by

$$x^a = \varepsilon y^a \quad X^A = \varepsilon Y^A \tag{9}$$

where ε is a small scalar that remains constant throughout the time history of deformation. Coarse- and fine-scale displacements $\mathbf{u}$ and $\mathbf{v}$, respectively, are introduced. These are restricted below to coincident Cartesian coordinate systems in the reference and spatial frames:

$$u^a = x^a - \delta^a_{.A} X^A \quad v^a = y^a - \delta^a_{.A} Y^A \tag{10}$$

with the Cartesian shifter $\delta^a_{.A} = 1$ for $a = A$ and $\delta^a_{.A} = 0$ for $a \neq A$. Corresponding deformation gradients then follow as

$$F^a_{.A} = \frac{\partial u^a}{\partial X^A} + \delta^a_{.A} \quad f^a_{.A} = \frac{\partial y^a}{\partial Y^A} + \delta^a_{.A} \tag{11}$$

Next an additive decomposition of displacements at the coarse scale is assumed:

$$u^a = \bar{u}^a + \tilde{u}^a = \bar{u}^a + \varepsilon \tilde{v}^a \tag{12}$$

where $\bar{u}^a$ represents the displacement that would exist in a microscopically homogeneous medium and $\tilde{u}^a$ is the perturbation in displacement due to fine-scale heterogeneity, with corresponding fine-scale representation $\tilde{v}^a$. The corresponding microscopic decomposition is

$$v^a = \varepsilon^{-1} u^a = \bar{v}^a + \tilde{v}^a = (F^a_{.A} - \delta^a_{.A}) Y^A + \tilde{v}^a \tag{13}$$

with $\bar{v}^a$ the microscopic displacement arising from the projection to the fine scale of the macroscopic deformation gradient $F^a_{.A}$. Differentiating $\mathbf{u}$ of Eq. (12) with respect to X^A gives

$$\frac{\partial}{\partial X^A} \left(\bar{u}^a + \varepsilon \tilde{v}^a\right) = \frac{\partial \bar{u}^a}{\partial X^A} + \frac{\partial \tilde{v}^a}{\partial Y^A} \tag{14}$$

where we have appealed to the second of Eq. (9). The left side of Eq. (8) can be written as follows in Cartesian coordinates:

$$\int\limits_V 2F^a_{.A} \frac{\partial \Psi}{\partial C_{AB}} g_{ab}(\delta u)^b_{|B} \, dV = \int\limits_V \frac{\partial \Psi}{\partial F^a_{.B}} \frac{\partial(\delta u^a)}{\partial X^B} dV \tag{15}$$

and the total displacement variation δu^a can be expressed, from Eq. (12), as

$$\delta u^a = \delta \bar{u}^a + \varepsilon \delta \tilde{v}^a \tag{16}$$

Substituting Eqs. (15) and (16) into Eq. (8) produces

$$\int\limits_V \frac{\partial \Psi}{\partial F^a_{.B}} \frac{\partial}{\partial X^B} (\delta \bar{u}^a + \varepsilon \delta \tilde{v}^a) dV$$

$$= \int\limits_{\partial V} T^a g_{ab}(\delta \bar{u}^b + \varepsilon \delta \tilde{v}^b) dA$$

$$+ \int\limits_V B^a g_{ab}(\delta \bar{u}^b + \varepsilon \delta \tilde{v}^b) dV \tag{17}$$

which is then volume averaged over microdomain Y to yield

$$\frac{1}{Y} \int\limits_Y \int\limits_V \frac{\partial \Psi}{\partial F^a_{.B}} \left(\frac{\partial(\delta \bar{u}^a)}{\partial X^B} + \frac{\partial(\delta \tilde{v}^a)}{\partial Y^B}\right) dV dY$$

$$= \frac{1}{Y} \int\limits_Y \int\limits_{\partial V} T^a g_{ab}(\delta \bar{u}^b + \varepsilon \delta \tilde{v}^b) dA dY$$

$$+ \frac{1}{Y} \int\limits_Y \int\limits_V B^a g_{ab}(\delta \bar{u}^b + \varepsilon \delta \tilde{v}^b) dV dY \tag{18}$$

Equation (18) is satisfied in the asymptotic limit $\varepsilon \to 0$ only if

$$
\frac{1}{Y}\iint_{Y\ V}\frac{\partial\Psi}{\partial F^a_{.B}}\frac{\partial(\delta\bar{u}^a)}{\partial X^B}dVdY=\int_{\partial V}T^ag_{ab}\delta\bar{u}^bdA \qquad (19)
$$

$$
+\int_V B^ag_{ab}\delta\bar{u}^bdV \ \ (\forall\delta\bar{u}^a)
$$

$$
\frac{1}{Y}\int_Y\int_V\frac{\partial\Psi}{\partial F^a_{.B}}\frac{\partial(\delta\tilde{v}^a)}{\partial Y^B}dVdY=0 \ \ (\forall\delta\tilde{v}^a) \qquad (20)
$$

Solutions of Eqs. (19) and (20) converge to the exact solution (i.e., minimum admissible system energy) for $\bar{u}^a$ and $\tilde{v}^a$ when the displacement field is periodic in Y, for example, when $\tilde{v}^a|_{Y=0} = \tilde{v}^a|_{Y=L}$ for a domain of size L. Note that $\bar{u}^a$ is constant over Y and thus automatically satisfies this periodicity constraint.

Equations (1)–(20) have addressed a purely continuum description at fine and coarse length scales. Presented next are kinematic and thermodynamic assumptions needed to relate atomistic and continuum fields and incrementally update atomic coordinates. Assume that in reference configuration B_0, the representative volume or unit cell for homogenization consists of atoms arranged in a lattice, perhaps imperfect due to the presence of defects. Furthermore, assume that in deformed configuration B, the same mass and number of atoms exist in this representative volume. The position vector for each atom j in configuration B_0 is given by $\mathbf{Z}_{\langle j\rangle} = a^i_{\langle j\rangle}\mathbf{E}_i$, where angled brackets are reserved for atomic labels which span 1 to $\mathbb{N}$, $a^i_{\langle j\rangle}$ are integers, and $\mathbf{E}_i$ are the lattice vectors in the reference configuration. Spatial positions $z^a_{\langle j\rangle}$ of atoms in configuration B are then found as follows, in Cartesian coordinates:

$$
z^a_{\langle j\rangle} = \delta^a_{.A}Z^A_{\langle j\rangle} + q^a_{\langle j\rangle} \qquad (21)
$$

with $\mathbf{q}_{\langle j\rangle}$ being a displacement vector between referential and current states for atom j. Let $\mathbf{R}_{\langle j\backslash k\rangle}$ and $\mathbf{r}_{\langle j\backslash k\rangle}$ denote vectors separating atoms j and k in respective configurations B_0 and B, that is,

$$
\mathbf{R}_{\langle j\backslash k\rangle} = \mathbf{Z}_{\langle k\rangle} - \mathbf{Z}_{\langle j\rangle} \qquad (22)
$$

$$
\mathbf{r}_{\langle j\backslash k\rangle} = \mathbf{z}_{\langle k\rangle} - \mathbf{z}_{\langle j\rangle} \qquad (23)
$$

The CB rule states that the atoms in the lattice match the gross deformation gradient $\bar{F}^a_{.A}$ of the continuum, $\mathbf{e}^a = \bar{F}^a_{.A}\mathbf{E}^A$, with $\mathbf{e}^a$ the lattice vectors in the deformed configuration. For certain crystals, namely, defect-free centrosymmetric crystals, this has been shown to be an effective means of representing crystal distortions [4]. However, symmetry-eliminating or symmetry-reducing features, such as crystal defects, invalidate CB and require an atomistic minimization computation, such as that advocated here in what follows, to determine distortions of local crystal structure near defects.

The point of departure here, therefore, is to use homogenization to determine a correction to the local region near the defect by approximating the new coordinates of the displaced lattice points with

$$
z^a_{\langle j\rangle} = \bar{F}^a_{\langle jk\rangle A}Z^A_{\langle k\rangle} + \tilde{v}^a_{\langle j\rangle} \qquad (24)
$$

with summation implied over repeated atomic indices. The first term on the right-hand side of Eq. (24), $\bar{F}^a_{\langle jk\rangle A}Z^A_{\langle k\rangle}$, accounts for the uniform projection over each periodic cell of the macroscopic lattice deformation field to the fine scale (i.e., the CB rule), and $\tilde{v}^a_{\langle j\rangle}$ is the discrete atomistic analog of the perturbation in displacement due to the microscopic heterogeneity given previously in Eq. (13), written here for atom j. Spatial separation vectors in Eq. (23) then become

$$
\mathbf{r}_{\langle j\backslash k\rangle}=\bar{\mathbf{F}}\mathbf{R}_{\langle j\backslash k\rangle}+\tilde{\mathbf{v}}_{\langle k\rangle}-\tilde{\mathbf{v}}_{\langle j\rangle}=\bar{\mathbf{F}}\mathbf{R}_{\langle j\backslash k\rangle}+\tilde{\mathbf{r}}_{\langle j\backslash k\rangle} \quad (25)
$$

with $\tilde{\mathbf{r}}_{\langle j\backslash k\rangle} = \tilde{\mathbf{v}}_{\langle k\rangle} - \tilde{\mathbf{v}}_{\langle j\rangle}$ accounting for deviations from the CB rule in a local sense.

Henceforth in the present work, we assume a free energy potential, measured either per unit reference volume or per atom, of the simple form depending only on the relative positions of atomic nuclei (Born-Oppenheimer lattice statics):

$$
\Psi = \Psi\left(\mathbf{q}_{\langle j\rangle}, \mathbf{Z}_{\langle j\rangle}\right)
$$
$$
= \Psi\left(\mathbf{r}_{\langle 1\backslash 2\rangle}, \mathbf{r}_{\langle 1\backslash 3\rangle}, \mathbf{r}_{\langle 2\backslash 3\rangle}, ... \mathbf{r}_{\langle \mathbb{N}-1\backslash\mathbb{N}\rangle}\right) \qquad (26)
$$

Interatomic forces $f_{\langle j\rangle a}$ and the Hessian matrix (i.e., atomic stiffness) $H_{\langle jk\rangle ab}$ are given by

$$
f_{\langle j\rangle a} = \frac{\partial\Psi}{\partial q^a_{\langle j\rangle}} \qquad H_{\langle jk\rangle ab} = \frac{\partial^2\Psi}{\partial q^a_{\langle j\rangle}\partial q^b_{\langle k\rangle}} \qquad (27)
$$

These quantities arise directly from a Taylor series expansion of Eq. (27) about a fixed set of reference coordinates $\mathbf{Z}_{\langle j\rangle}\big|_0$ comprising a perfect lattice:

$$
\Psi(\mathbf{q}_{\langle j\rangle})=\Psi_0+f_{\langle k\rangle a}\big|_0\,q^a_{\langle k\rangle}+\tfrac{1}{2}\,H_{\langle jk\rangle ab}\big|_0\,q^a_{\langle j\rangle}q^b_{\langle k\rangle}+\cdots \ (28)
$$

where the subscript 0 denotes quantities evaluated at $\mathbf{q}_{\langle j \rangle} = \mathbf{0}$. The expansion of the strain energy potential of the solid about the undeformed state is also given by the following continuum approximation:

$$\Psi\left(F^a_{.A}\right) = \Psi_0 + \left.\frac{\partial \Psi}{\partial F^a_{.A}}\right|_{\delta^a_{.A}} \left(F^a_{.A} - \delta^a_{.A}\right) \tag{29}$$

$$+ \frac{1}{2} \left.\frac{\partial^2 \Psi}{\partial F^a_{.A} \partial F^b_{.B}}\right|_{\delta^a_{.A}} \left(F^a_{.A} - \delta^a_{.A}\right)\left(F^b_{.B} - \delta^b_{.B}\right) + \cdots$$

where the reference energy Ψ_0 is typically assigned a value of zero in strictly continuum models. Note that a more specific objective form of Eq. (29) could be written in terms of the strain measure E_{AB} of Eq. (6), for example, as opposed to the deformation gradient $F^a_{.A}$. While only the former is invariant under rigid body motion, Eq. (29) suffices, for illustrative purposes, in the present context. On taking the first variations of Eqs. (28) and (29), atomic forces and stresses vanish in a perfect lattice in the undeformed state, that is,

$$f_{\langle j \rangle a}\big|_0 = 0 \qquad \left.\frac{\partial \Psi}{\partial F^a_{.A}}\right|_{\delta^a_{.A}} = 0 \tag{30}$$

leaving the following force-displacement and stress-deformation relations on neglecting higher than second-order terms in Eqs. (28) and (29):

$$f_{\langle j \rangle a} = H_{\langle jk \rangle ab}\big|_0 q^b_{\langle k \rangle} \qquad P^{.A}_a = \left.\hat{\mathbb{C}}^{AB}_{ab}\right|_{\delta^a_{.A}} \left(F^b_{.B} - \delta^b_{.B}\right) \tag{31}$$

where the mixed-configurational elastic moduli are $\hat{\mathbb{C}}^{AB}_{ab} = \partial^2\Psi/\partial F^a_{.A}\partial F^b_{.B}$. Unobstructed minimization of Eqs. (28) and (29) may proceed only when $H_{\langle jk \rangle ab}$ and $\hat{\mathbb{C}}^{AB}_{ab}$ are positive semidefinite functions of their arguments. Using Eq. (30) and equating reference energies Ψ_0 in Eqs. (28) and (29), to second order,

$$H_{\langle jk \rangle ab} q^a_{\langle j \rangle} q^b_{\langle k \rangle} = \hat{\mathbb{C}}^{AB}_{ab}\left(F^a_{.A} - \delta^a_{.A}\right)\left(F^b_{.B} - \delta^b_{.B}\right) \tag{32}$$

a relation that is generalized here to hold when $H_{\langle jk \rangle ab}$ and $\hat{\mathbb{C}}^{AB}_{ab}$ are not evaluated at the reference state (i.e., secant moduli) and when the lattice is not initially free of defects. Integrating the right-hand side of Eq. (15) by parts and applying the divergence theorem over volume Y with oriented surface element $N_A dA$,

$$\frac{1}{A}\int\limits_{\partial Y}\int\limits_V \frac{\partial \Psi}{\partial F^a_{.A}}\delta\tilde{v}^a N_A dV dA$$

$$= \frac{1}{Y}\int\limits_Y\int\limits_V \frac{\partial}{\partial Y^A}\left(\frac{\partial \Psi}{\partial F^a_{.A}}\right)\delta\tilde{v}^a dV dY \tag{33}$$

Localizing the volume integral on the right-hand side of Eq. (33) and considering all admissible variations $\delta\tilde{\mathbf{v}}$, the microscopic linear momentum balance becomes

$$\frac{\partial}{\partial Y^A}\left(\frac{\partial \Psi}{\partial F^a_{.A}}\right) = \frac{\partial P^{.A}_a}{\partial Y^A} = 0 \;\; (\text{in } Y) \tag{34}$$

as the area integral vanishes since one may select $\delta\tilde{\mathbf{v}} = \mathbf{0}$ on $A = \partial Y$. Equation (34) is general in the sense that no assumption is made on the order of the incremental elastic response; for example, nonlinear higher-order elastic constants are admitted. For algorithmic purposes, however, it is advantageous to assume a first-order hyperelastic response along the lines of Eq. (31), an appropriate assumption for most engineering metals undergoing quasi-static deformations:

$$\frac{\partial}{\partial Y^A}\left(\hat{\mathbb{C}}^{AB}_{ab}\left(F^b_{.B} - \delta^b_{.B}\right)\right) = 0 \tag{35}$$

where $\hat{\mathbb{C}}^{AB}_{ab}$ is a mixed-variant effective elastic modulus tensor. Next, from Eq. (11) and the displacement gradient expression Eq. (14), Eq. (35) becomes

$$-\frac{\partial\hat{\mathbb{C}}^{AB}_{ab}}{\partial Y^A}\left(\frac{\partial\bar{u}^b}{\partial X^B}\right) = \frac{\partial}{\partial Y^A}\left(\hat{\mathbb{C}}^{AB}_{ab}\frac{\partial\tilde{v}^b}{\partial Y^B}\right) \tag{36}$$

The intention of the present derivation is expression of Eq. (36) in terms of atomistic and macroscopic displacements. Invoking the chain rule gives

$$\frac{\partial}{\partial Z^B_{\langle j \rangle}} = \frac{\partial Y^A}{\partial Z^B_{\langle j \rangle}}\frac{\partial}{\partial Y^A} = \delta^A_{\langle j \rangle B}\frac{\partial}{\partial Y^A} \tag{37}$$

where the linear operator $\delta^A_{\langle j \rangle B}$ simply refers initial position $Z^B_{\langle j \rangle}$ of discrete atom j to fine scale reference coordinate Y^A. On inserting Eq. (37) into the left-hand side of Eq. (36),

$$\frac{\partial\hat{\mathbb{C}}^{AB}_{ab}}{\partial Y^A}\left(\frac{\partial\bar{u}^b}{\partial X^B}\right) \rightarrow \frac{\partial\hat{\mathbb{C}}^{AB}_{ab}}{\partial Z^A_{\langle j \rangle}}\left(\frac{\partial\bar{u}^b}{\partial X^B}\right)$$

$$= \frac{\partial^2\Psi}{\partial q^a_{\langle j \rangle}\partial F^b_{.B}}\left(\frac{\partial\bar{u}^b}{\partial X^B}\right) = -D^B_{\langle j \rangle ab}\left(\frac{\partial\bar{u}^b}{\partial X^B}\right) \tag{38}$$

where $D^A_{\langle j \rangle ab} = -\partial^2 \Psi / \partial q^a_{\langle j \rangle} \partial F^b_{.A}$. On appealing to Eq. (32), and assuming small atomic perturbations $\tilde{v}^a_{\langle m \rangle}$, the right-hand side of Eq. (36) becomes

$$\frac{\partial}{\partial Y^A} \left(\hat{\mathbb{C}}^{AB}_{ab} \frac{\partial \tilde{v}^b}{\partial Y^B} \right) \rightarrow \frac{\partial}{\partial Z^A_{\langle k \rangle}} \left(\hat{\mathbb{C}}^{AB}_{ab} \frac{\partial \tilde{v}^b_{\langle k \rangle}}{\partial Z^B_{\langle j \rangle}} \right)$$

$$= \frac{\partial^2 \Psi}{\partial q^a_{\langle k \rangle} \partial q^b_{\langle j \rangle}} \tilde{v}^b_{\langle k \rangle} = H_{\langle kj \rangle ab} \tilde{v}^b_{\langle k \rangle} \qquad (39)$$

In Eqs. (38) and (39), the $\rightarrow$ notation denotes the transformation steps $\tilde{v}^b \rightarrow \tilde{v}^b_{\langle k \rangle}$ and $\delta^A_{.B} \rightarrow \delta^A_{\langle j \rangle B}$. Using Eqs. (38) and (39), the fine-scale equilibrium Eq. (36) finally becomes

$$D^A_{\langle j \rangle ab} \frac{\partial \bar{u}^b}{\partial X^A} = H_{\langle kj \rangle ab} \tilde{v}^b_{\langle k \rangle} \qquad (40)$$

Subsequently, Eq. (40) is solved for the inner displacements $\tilde{v}^b_{\langle k \rangle}$ describing the locally perturbed atomic coordinates. Note that by hypothesis and analogy with the two-scale continuum homogenization theory, solution of Eq. (40) converges to the exact solution (i.e., lowest-energy configuration of admissible sets of atomic coordinates) only when $\tilde{v}^b_{\langle k \rangle}$ is periodic over Y. In other words, periodic boundary conditions on atomic displacements [74] must be applied at the fine scale for Eq. (40) to yield a meaningful solution.

Now reconsider coarse-scale Eq. (19), assuming that $\tilde{\mathbf{v}}$ is known from solution of Eq. (40). The left-hand side of Eq. (19) can be written as

$$\frac{1}{Y} \int_Y \int_V \frac{\partial \Psi}{\partial F^a_{.B}} \frac{\partial (\delta \bar{u}^a)}{\partial X^B} dV dY \qquad (41)$$

$$= \frac{1}{Y} \int_Y \int_V \hat{\mathbb{C}}^{BA}_{ab} \left(\frac{\partial \bar{u}^b}{\partial X^A} + \frac{\partial \tilde{v}^b}{\partial Y^A} \right) \frac{\partial (\delta \bar{u}^a)}{\partial X^B} dV dY$$

where fine-scale atomic coordinates affect $F^a_{.A}$ and $\hat{\mathbb{C}}^{AB}_{ab}$ through Eqs. (14) and (28), respectively, and thus affect the macroscopic response. From Eqs. (37)–(40),

$$\hat{\mathbb{C}}^{BA}_{ab} \frac{\partial \tilde{v}^b}{\partial Y^A} \rightarrow \hat{\mathbb{C}}^{BA}_{ab} \frac{\partial \tilde{v}^b_{\langle j \rangle}}{\partial \tilde{Z}^A_{\langle j \rangle}} = \frac{\partial^2 \Psi}{\partial q^a_{\langle j \rangle} \partial F^b_{.B}} \tilde{v}^b_{\langle j \rangle}$$

$$= -D^B_{\langle j \rangle ab} \tilde{v}^b_{\langle j \rangle} \qquad (42)$$

The coarse-scale, static linear momentum balance, Eq. (19), then becomes

$$\frac{1}{Y} \int_Y \int_V \hat{\mathbb{C}}^{BA}_{ab} \left(\frac{\partial \bar{u}^b}{\partial X^A} \right) \frac{\partial (\delta \bar{u}^a)}{\partial X^B} dV dY = \int_{\partial V} T^a g_{ab} \delta \bar{u}^b dA$$

$$+ \int_V B^a g_{ab} \delta \bar{u}^b dV + \frac{1}{Y} \int_Y \int_V D^B_{\langle j \rangle ab} \tilde{v}^b_{\langle j \rangle} \frac{\partial (\delta \bar{u}^a)}{\partial X^B} dV dY \quad (43)$$

3. IMPLEMENTATION

The focus of the present effort is application of Eq. (40) to update the configuration of $\mathbb{N}$ atoms subjected to macroscopic displacement gradient $\partial \bar{u}^b / \partial X^A$, applied uniformly over a single coarse-scale integration point, such that Eq. (43) need not be solved explicitly. The atoms comprise a periodic unit cell of volume Y and may be arranged initially to encompass defects, such as vacancies or dislocations, at $t = 0$. Perturbations from homogeneous deformation (i.e., perturbations from the CB) are measured by the atomic quantity $\tilde{v}^b_{\langle j \rangle}$. Note that when the CB is accurate, for example, when defects are absent, the macroscopic stress at a given applied deformation level is minimized with respect to variations in atomic degrees of freedom such that $\partial (\partial \Psi / \partial F^a_{.A}) / \partial q^b_{\langle j \rangle} = 0$, and thus Eq. (40) yields $\tilde{v}^b_{\langle j \rangle} = 0$.

Since the material's mechanical response is nonlinear in the presence of defects, an iterative scheme is employed for application of the AEH computational method to deforming crystals. Let S be the enumerated set of all conceivable nonuniform deformations of the lattice:

$$z^a_{\langle j \rangle} \Big|^i = \bar{F}^a_{\langle jk \rangle A} Z^A_{\langle k \rangle} + \eta^i \tilde{v}^a_{\langle m \rangle} \quad (\forall i \in S) \qquad (44)$$

Equilibrium Eq. (40) then becomes

$$D^A_{\langle j \rangle ab} \frac{\partial \bar{u}^b}{\partial X^A} \Big|^i = H_{\langle jk \rangle ab} \eta^i \tilde{v}^b_{\langle k \rangle} \qquad (45)$$

where the line search parameter η^i is determined iteratively such that a local minimum-energy configuration is attained:

$$\min_{\eta^i} \Psi \left(\mathbf{z} \left(\eta^i \right) \right) \approx \min_{\mathbf{q}_{\langle j \rangle}} \Psi \left(\mathbf{z} \left(\mathbf{q}_{\langle j \rangle} \right) \right) \qquad (46)$$

The physical implication of Eq. (46) is that the minimum energy state corresponding to the vector $\mathbf{q}_{\langle j \rangle}$ of Eq. (21) can be approximated by the state that corresponds to Eq. (44), where the information in

the initial solution vector $\tilde{v}^b_{\langle k \rangle}$, determined earlier in the computation from Eq. (40), has been reused. A scenario in which such a scheme may offer significant computational benefit is mechanical calculations of lattice deformations for generating stress-strain curves, whereby the deformation gradient is monotonically increased.

The numerical algorithm proceeds as follows. First, Eq. (40) provides the trajectory for $\tilde{v}^b_{\langle k \rangle}$ in $3 \times \mathbb{N}$ solution space. Then atomic coordinates $\mathbf{z}_{\langle j \rangle}$ and corresponding displacements $\mathbf{q}_{\langle j \rangle}$ are updated iteratively via Eq. (44). With each iteration, the energy $\Psi\left(\mathbf{z}\left(\mathbf{q}_{\langle j \rangle}\right)\right)$ is computed using the updated coordinates $\mathbf{z}_{\langle j \rangle} = \mathbf{Z}_{\langle j \rangle} + \mathbf{q}_{\langle j \rangle}$. A bisection algorithm is used to efficiently determine the particular value of η^i that gives the minimum energy condition $\partial \Psi\left(\mathbf{z}\left(\eta^i\right)\right)/\partial \eta^i = 0$ for each increment in macroscopic deformation $\bar{\mathbf{u}}$.

The noteworthy feature of the present AEH computational method is its straightforward trajectory, determined by Eq. (45), to the solution of updated atomic coordinates and the corresponding energy minimum. This is in contrast to traditional molecular dynamics simulations that rely on a series of incremental loading and equilibration steps or CGM methods that rely on series of incremental straining and minimization steps, both in full $3 \times \mathbb{N}$ solution space. The methods are compared qualitatively in Fig. 1. For the molecular methods, the stepwise solution path denotes successive incremental loading and relaxation. For the AEH method, the trajectory of the solution is denoted by the corresponding dotted line, with distance along this path mea-

sured in practice by the value of line search parameter η^i. It is also important to note that no assumption of linearity of material behavior is made. Indeed, the determination of the numerical value η^i through the condition $\partial \Psi\left(\mathbf{z}\left(\eta^i\right)\right)/\partial \eta^i = 0$ leaves the full material nonlinear (or nonquadratic) features of the atomistic energy Ψ undisturbed.

The AEH method is applied here in a study of the mechanical behavior of pure tungsten (W), a BCC transition metal of relatively high mass density. Its combination of high density, high strength, and high melting point render it a popular material for use in defense applications such as ordnance [63,75]. The potential energy function used here for describing atomistic interactions in W is discussed in what follows.

An empirical $\mathbb{N}$-body potential specifically developed for transition metals [76] is used to compute the free energy Ψ of Eq. (26), in particular because of its adequacy for describing energies and/or motion of dislocations and other lattice defects in W, as reported elsewhere [77–80]. According to the representation of Finnis and Sinclair [76], the summed total potential energy E of a set of atoms at positions $\{\mathbf{z}_{\langle j \rangle}\}$ for $j = 1, 2, ..., \mathbb{N}$ is given by

$$E = E_N + E_P \qquad (47)$$

where E_N is the $\mathbb{N}$-body term that is a function of the superposition of the local electronic charge densities $\rho_{\langle j \rangle}$, the latter obtained from summation of atomic charge densities ϕ. E_P is a pair potential that accounts for core-core interactions. Specifically, the $\mathbb{N}$-body term is

$$E_N = -\Lambda \sum_{\langle j \rangle} f\left(\rho_{\langle j \rangle}\right) \qquad (48)$$

where

$$f\left(\rho_{\langle j \rangle}\right) = \sqrt{\rho_{\langle j \rangle}} \quad \rho_{\langle j \rangle} = \sum_k \phi\left(r_{\langle j \backslash k \rangle}\right) \qquad (49)$$

is always nonnegative and real,

$$r_{\langle j \backslash k \rangle} = \left|\mathbf{r}_{\langle j \backslash k \rangle}\right| = \left|\mathbf{z}_{\langle k \rangle} - \mathbf{z}_{\langle j \rangle}\right| \qquad (50)$$

$$\phi\left(r\right) = \begin{cases} (r-d)^2, \ r \leq d \\ 0, \ r > d \end{cases} \qquad (51)$$

and Λ is an empirical constant. The parameter d denotes an adjustable cutoff zone for superposition of local charge densities, chosen here to lie between the
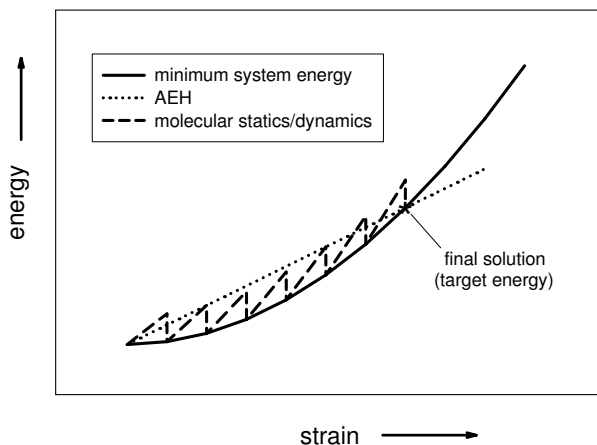

FIGURE 1. Schematic comparison of numerical approaches

second and third nearest neighbors, that is, $a < d < a\sqrt{2}$, with a the lattice parameter. The pair potential is constructed as

$$E_P = \frac{1}{2} \sum_{j,k,j \neq k} \psi \left(r_{\langle j \backslash k \rangle} \right) \tag{52}$$

where ψ is of the following polynomial form:

$$\psi \left(r \right) = \begin{cases} (r - c)^2 \left(c_0 + c_1 r + c_2 r^2 \right), & r \leq c \\ 0, & r > c \end{cases} \tag{53}$$

with empirical constants c_0, c_1, and c_2. The cutoff parameter c, like d of Eq. (51), is also assigned a value between the second and third nearest neighbor distances. Finnis and Sinclair [76] determined the other constants via calibration to experimentally determined, macroscopic elastic properties for single crystalline W. Tables 1 and 2 list the experimental and fitted parameters, respectively.

Notice that E is the total energy of $\mathbb{N}$ atoms in the fine-scale unit cell. The Helmholtz free energy density in a continuum sense, Ψ, is related to E as

$$\Psi = U - \eta\theta = \frac{E}{\beta\mathbb{N}} \tag{54}$$

where U is the continuum internal energy, η is the continuum entropy per unit volume, and θ is the absolute thermodynamic temperature of the system, which we assume is zero in the last of Eq. (54) for the present implementation in the context of molecular statics, such that $E = \beta\mathbb{N}U$. Also included in Eq. (54) is the scalar $\beta = 0.5a^3$, a constant denoting the volume occupied by each atom in a perfect reference lattice. This unit conversion factor was included implicitly in earlier work [45].

Substitution of Eqs. (47) and (54) into earlier definitions then yields

$$H_{\langle jk \rangle ab} = \frac{\partial^2 \Psi}{\partial q^a_{\langle j \rangle} \partial q^b_{\langle k \rangle}} = \frac{1}{\beta\mathbb{N}} \left[\frac{\partial^2 (\mathrm{E}_N + \mathrm{E}_P)}{\partial q^a_{\langle j \rangle} \partial q^b_{\langle k \rangle}} \right] \tag{55}$$

$$D^A_{\langle j \rangle ab} = -\frac{\partial^2 \Psi}{\partial q^a_{\langle j \rangle} \partial F^b_{.A}} = -\frac{1}{\beta\mathbb{N}} \frac{\partial^2 (\mathrm{E}_N + \mathrm{E}_P)}{\partial q^a_{\langle j \rangle} \partial q^c_{\langle k \rangle}} \frac{\partial q^c_{\langle k \rangle}}{\partial F^b_{.A}} \tag{56}$$

$$\hat{\mathbb{C}}^{AB}_{ab} = \frac{\partial^2 \Psi}{\partial F^a_{.A} \partial F^b_{.B}} = \frac{1}{\beta\mathbb{N}} \frac{\partial^2 (\mathrm{E}_N + \mathrm{E}_P)}{\partial q^c_{\langle j \rangle} \partial q^d_{\langle k \rangle}} \frac{\partial q^c_{\langle j \rangle}}{\partial F^a_{.A}} \frac{\partial q^d_{\langle k \rangle}}{\partial F^b_{.B}} \tag{57}$$

To first order, from Eqs. (21)–(25), with $\bar{F}^a_{\langle jk \rangle A} \approx F^a_{.A}\delta_{\langle jk \rangle}$, the following geometric relationships arise:

$$\frac{\partial r^c_{\langle j \backslash k \rangle}}{\partial F^a_{.A}} = R^A_{\langle j \backslash k \rangle} \delta^c_{.a} \quad \frac{\partial q^b_{\langle j \rangle}}{\partial F^a_{.A}} = Z^A_{\langle j \rangle} \delta^b_{.a} \tag{58}$$

Derivatives of E with respect to atomic displacements $q^a_{\langle j \rangle}$ are listed in [76] and are not repeated here. In the present numerical scheme, Eqs. (55)–(58) are evaluated analytically and subsequently used in fine-scale equilibrium Eq. (45).

4. NUMERICAL RESULTS AND VALIDATION

The AEH multiscale computational method is applied here to address the nonlinear elastic response of body-centered cubic (BCC) tungsten (W) containing periodically distributed vacancies and screw dislocations of two orientations. In these simulations, unit cells are deformed in uniaxial stretch to 2.5% elongation. The primary solution variable of interest is the strain energy density of the material in the presence of defects contained within the unit cell. The present approach readily enables parametric variations of the defect density via the prescription of the number of atoms in the fine-scale representation relative to the total number of defects embedded within the unit cell.

One intention of the present investigation, discussed in more detail in Section 5, is examination of aspects of material behavior that could be used subsequently in stand-alone continuum defect theories, in particular, details associated with stored energy of defect fields and the effects of applied deformations on elasticity and stored energy for various fixed defect concentrations. Despite the presumption of zero temperature, one may still draw conclusions, at least in a qualitative sense, regarding stress and energetics associated with dislocation behavior in BCC metals in the context of lattice statics calculations [74,78]. A standard trend in the literature has been development of such scaling methods for the purely mechanical problem before extending to the finite temperature regime [81].

Simulations of the deformation of unit cells containing various numbers of atoms, configured to represent several classes of crystal defects, are conducted. In the calculations, the energy density and tangent stiffness of a single Lagrangian finite element integration point are determined by the microscopic (i.e., atomistic) response. Initial atomic coordinates are found using a two-step procedure: first the linear-elastic solution for displacement field

TABLE 1. Experimental lattice quantities for W

a	Lattice parameter [Å]	3.1652
E^C	Cohesive energy [eV/atom]	-8.90
C_{11}	Elastic constant [GPa]	522.4
C_{12}	Elastic constant [GPa]	204.4
C_{44}	Rhombohedral shear modulus [GPa]	160.6
μ	Tetragonal shear modulus [GPa]	159.0
B	Bulk modulus [GPa]	310.4
P^C	Cauchy pressure $=\frac{1}{2}\left(C_{12} - C_{44}\right)$ [GPa]	21.9

TABLE 2. Constants for Finnis-Sinclair [76] EAM potential (W)

d [Å]	4.40024
Λ[eV]	1.896373
c [Å]	3.25
c_0	47.1346499
c_1	-33.7665655
c_2	6.2541999

of the defect is applied to the atoms, then a conjugate gradient algorithm [49] is invoked to transition the atomic positions to a stable local minimum energy state. Subsequently, the response to applied deformation is computed using our AEH scheme according to the numerical procedure described in Section 3. The applied (i.e., coarse scale) deformation gradient field (in conjunction with fine-scale periodicity) is uniaxial stretching over a range of $1.000 \leq F_{11} \leq 1.025$, with the lateral edges fixed (covariant Cartesian notation is used here and in subsequent figures for simplicity, i.e., $\bar{F}^1_{.1} \rightarrow F_{11}$). We also compare, for validation purposes, the final configurations attained using our procedure with those obtained from incremental energy minimization using the CGM method. In the latter approach, a small increment in the stretch field is first imposed uniformly over all atoms, and then a conjugate gradient program [49] is used to update the atomic coordinates to the corresponding local minimum energy state. This process continues, with a new set of conjugate gradient minimization iterations conducted on application of each successive stretch increment, until the final, fully deformed configuration is reached.

Two orientations of atomistic unit cells are investigated. In the first, shown in Fig. 2, the axis of applied stretch is oriented along the [111]-direction in the lattice. Here the BCC unit cell is a rectangle of dimensions $L_1 \times L_2 \times L_3 = a\sqrt{3}N_1 \times a\sqrt{6}N_2 \times a\sqrt{2}N_3$,

where N_1, N_2, and N_3 are, respectively, the number of repeating planes stacked in the [111]-, [11$\bar{2}$]-, and [1$\bar{1}$0]-directions. In the second orientation (not shown), the axis of applied stretch is oriented along the [100]-direction in the lattice, and the unit cell is of dimensions $L_1 \times L_2 \times L_3 = aN_1 \times aN_2 \times aN_3$, where N_1, N_2, and N_3 are, respectively, the number of repeating planes stacked in the [100]-, [010]-, and [001]-directions. Periodic boundary conditions [74] are applied along all faces of the unit cell such that atoms exiting the unit cell during the calculation are mapped back into the cell on the opposite face, thereby preserving the total mass of the system. Table 3 lists the details pertaining to specific
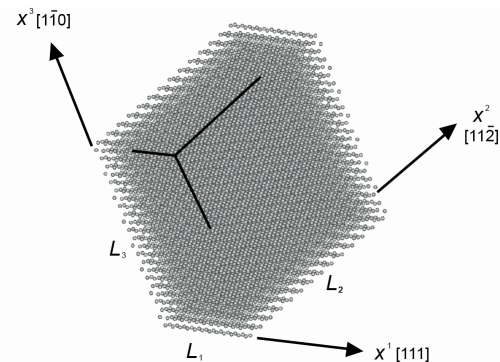

FIGURE 2. Atomic scale unit cell for BCC lattice (defect-free [111] configuration shown)

TABLE 3. Unit cell parameters for energy minimization computations

Case #	Defect	Lattice orientation	Atoms $\mathbb{N}$	Unit cell size $L_1 \times L_2 \times L_3$ [nm]	Vacancy conc. χ	Burgers vector $|\mathbf{b}|$[nm]	Disl. density α^{11} [1/nm]
1	vacancy	[111]	2016	$3.29 \times 3.10 \times 3.13$	$5.0(10)^{-4}$	-	-
2	vacancy	[111]	8064	$3.29 \times 6.20 \times 6.27$	$1.2(10)^{-4}$	-	-
3	vacancy	[111]	18144	$3.29 \times 9.30 \times 9.40$	$5.5(10)^{-5}$	-	-
4	vacancy	[111]	32256	$3.29 \times 12.4 \times 12.5$	$3.1(10)^{-5}$	-	-
5	dislocation	[111]	8064	$3.29 \times 6.20 \times 6.27$	-	0.27411	0.0071
6	dislocation	[111]	18144	$3.29 \times 9.30 \times 9.40$	-	0.27411	0.0031
7	dislocation	[111]	32256	$3.29 \times 12.4 \times 12.5$	-	0.27411	0.0018
8	dislocation	[100]	2000	$3.17 \times 3.17 \times 3.17$	-	0.31652	0.0316
9	dislocation	[100]	8000	$3.17 \times 6.33 \times 6.33$	-	0.31652	0.0079
10	dislocation	[100]	18000	$3.17 \times 9.50 \times 9.50$	-	0.31652	0.0035
11	dislocation	[100]	32000	$3.17 \times 12.7 \times 12.7$	-	0.31652	0.0020

unit cells investigated in this work and discussed in what follows.

First considered are vacancies. The corresponding initial configuration is constructed simply by removing the atom closest to the centroid of the unit cell. The defect density in this case is defined as the volume fraction of missing atoms, that is, $\chi = 1/\mathbb{N}$, where $\mathbb{N}$ is the total number of atoms prior to vacancy creation, ranging from 2016 to 32,256 among the simulations listed in Table 3. Defect energy is shown in Fig. 3, defined on a per-atom basis as
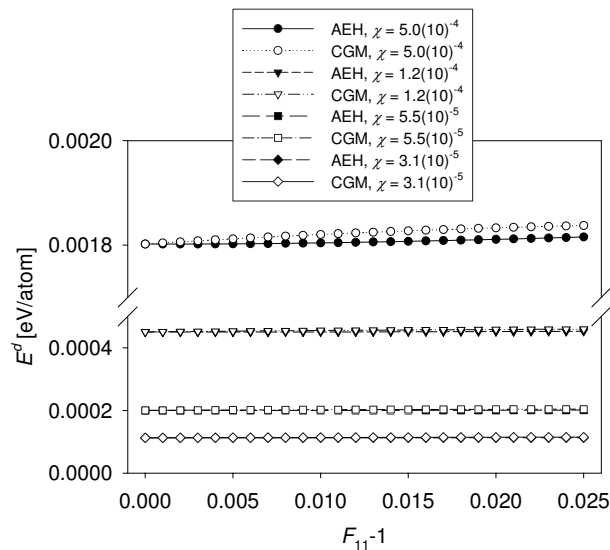

FIGURE 3. Defect energy versus applied stretch for unit cells with vacancy concentration χ. Energies computed using current AEH method and CGM method [49]

$$E^d = \frac{E - \bar{E}}{\mathbb{N}} \tag{59}$$

where E is the total potential energy of the system from Eq. (47) and $\bar{E}$ is the total potential energy of a perfect BCC W lattice of the same dimensions and same number of atoms (prior to vacancy formation), subjected to the same deformation boundary conditions. From Fig. 3, we see that the AEH approach is validated in the sense that it predicts minimum energy atomic configurations that compare favorably with those obtained using incremental conjugate gradient minimization (CGM). Compared in Table 4 are the total vacancy energies $\mathbb{N}E^d$ at an applied deformation of $F_{11} = 1.025$ (2.5% uniaxial strain), computed by AEH, CGM, and the CB rule. In these calculations, AEH predicted the lowest energy, followed by CGM, with CB predicting the highest energy. Recall that all three methods commenced from the same set of initial atomic coordinates, found via energy minimization from CGM at $F_{11} = 1.000$. For the CB, the atoms were displaced homogeneously, via F_{11}, from their initial coordinates without any energy minimization or correction, leading naturally to a higher defect energy than was achieved via the other two methods. Notice from Fig. 3 that the defect energy increases with applied stretch F_{11}. Furthermore, from Table 4, the energy per vacancy under applied deformation decreases with decreasing defect density χ. Schultz [82] reported an experimental value of 3.6 eV for vacancy formation energy in pure W at null applied strain.

TABLE 4. Vacancy energies at applied stretch $F_{11} = 1.025$, computed by asymptotic expansion homogenization (AEH), conjugate gradient minimization (CGM), and the Cauchy-Born approximation (CB)

Case #	Defect density χ	$\mathbb{N}E^d$[ev], $F_{11} = 1.025$		
		AEH	CGM	CB
1	$5.0(10)^{-4}$	3.6603	3.7046	3.7203
2	$1.2(10)^{-4}$	3.6492	3.7032	3.7189
3	$5.5(10)^{-5}$	3.6456	3.7030	3.7187
4	$3.1(10)^{-5}$	3.6439	3.7029	3.7186

Considered next is the energy of W containing periodic arrays of screw dislocations. Two types of screw dislocations are modeled. In the first type (cases 5–7 in Table 3), the dislocation tangent line and Burgers vector **b** are oriented along the [111]-direction and pass through the centroid of the unit cell, with $b = |\mathbf{b}| = \sqrt{3}a/2$. This class of $a/2\langle 111 \rangle$ dislocations, most prevalent in BCC metals such as W, is thought to dominate strain hardening behavior in plastic deformation and has received the most attention in the molecular mechanics literature [74,78,80,83]. In the second type (cases 8–11 in Table 3), the tangent line and Burgers vector are oriented along the [100]-direction and pass through the centroid of the unit cell, with $b = |\mathbf{b}| = a$. Such $a\langle 100 \rangle$ dislocations, while of less general interest than the aforementioned $a/2\langle 111 \rangle$ type, have been observed in BCC metals [83], but usually as part of hexagonal networks, emerging as a result of attractive junctions between two $a/2\langle 111 \rangle$ dislocations. Nonetheless, the $a\langle 100 \rangle$ dislocations are of interest here since they provide another class of defect whose behavior may be used to verify the accuracy of the AEH method, and may later be parameterized in a continuum setting. In either case, initial atomic positions, prior to minimization at null strain via CGM, are prescribed via the usual displacement field attributed to a screw dislocation embedded in an infinite isotropic elastic body: $u^1 = b\hat{\theta}/2\pi$, where $\hat{\theta}$ is an angular coordinate about the axis of the dislocation line. Note that the isotropic solution should be particularly valid for tungsten as single crystalline W is virtually elastically isotropic [84]. The scalar dislocation density is defined as the defect line length per unit reference volume, here $\bar{\rho} = 1/(L_2 L_3)$, and the dislocation density tensor [85] becomes, in this context,

$$\alpha^{AB} = \bar{\rho} b^A \xi^B \qquad (60)$$

where ξ is the unit tangent line in the reference configuration. Note that α denotes the density of GNDs in the sense of Ashby [62]. For the present set of simulations of screw dislocations, $\mathbf{b} \parallel \xi$, and the only nonvanishing component of α is $\alpha^{11} = b/(L_2 L_3)$.

The core structure for an $a/2\langle 111 \rangle$ screw dislocation, prior to applied loading, is shown in Fig. 4(a). In this two-dimensional illustration of the stacking sequence of {111} planes, the relative [111] displacements of atoms are denoted by arrows, with the size of each arrow denoting the magnitude of the relative displacement [74,86]. The results shown for the equilibrium undeformed structure of the dislocation core are consistent with the findings in earlier literature [74,83], thereby validating the initial conditions used in the present set of simulations. The following observations are made: (1) the differential displacements exhibit threefold symmetry about the dislocation core; (2) the largest displacements occur along the {110} planes, directed radially away from the core, with decreasing magnitude on increasing distance from the core; and (3) displacements of other atoms in the system do not exhibit reflection symmetry about the {110} planes. Dislocation energies per atom, computed via AEH and CGM, are compared in Fig. 4(b) for $a/2\langle 111 \rangle$ dislocations and in Fig. 4(c) for $a\langle 100 \rangle$ dislocations. The defect energy per atom is defined as in Eq. (59), that is, $E^d = (E - \bar{E})/\mathbb{N}$, where E is the total potential energy of the system and $\bar{E}$ is the total potential energy of a perfect BCC W lattice of the same dimensions and same number of atoms, subjected to the same deformation boundary conditions. This quantity is computed accurately by AEH, as is verified by close agreement with the incremental conjugate gradient (CGM) solutions, as shown in Figs. 4(b) and 4(c). Note, however, that AEH appears to perform better (i.e., yields a lower result for E^d rela-
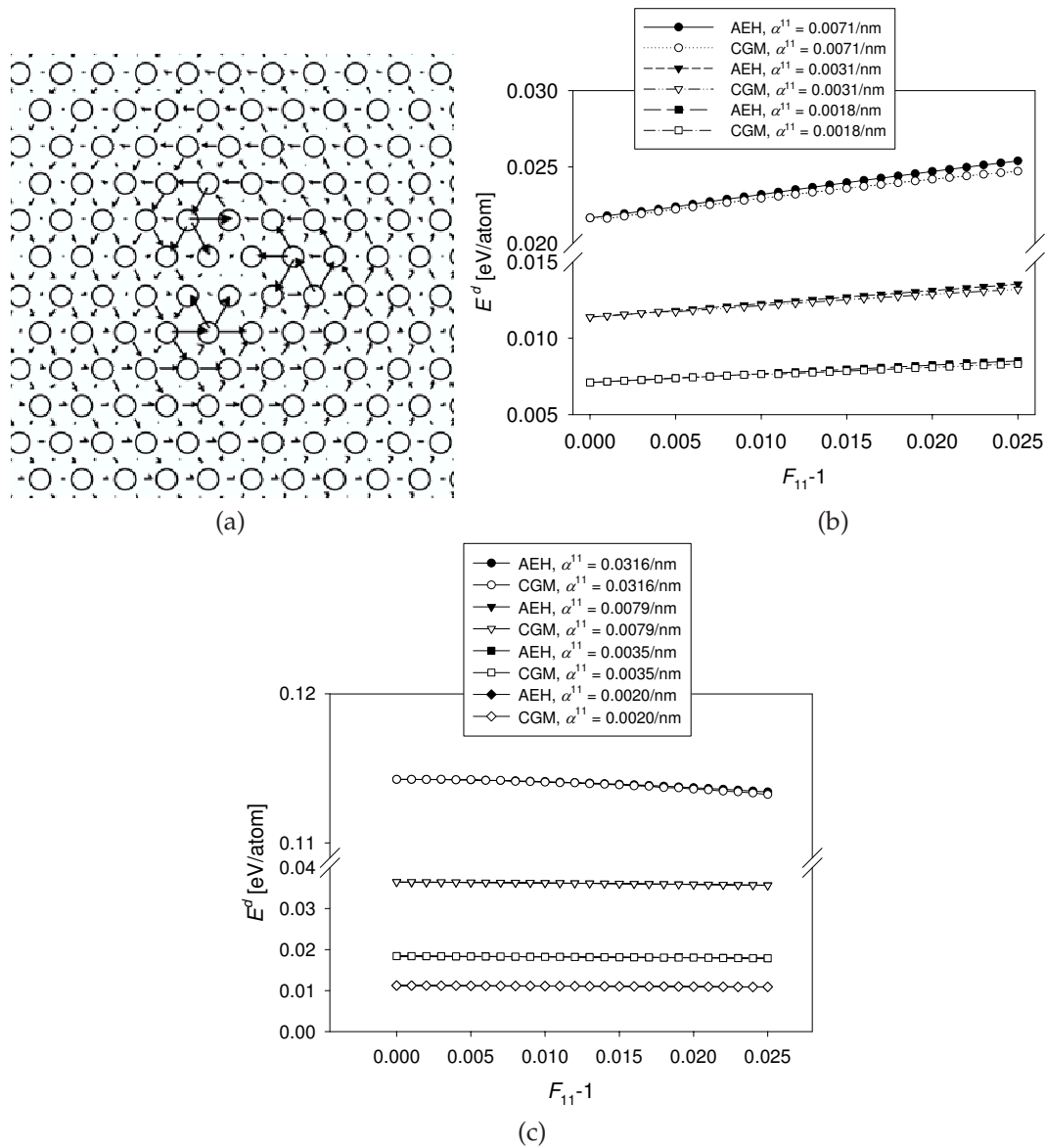
FIGURE 4. Screw dislocation results. **a)** [111] differential displacement map for $a/2 \langle 111 \rangle$ screw dislocation [74,86], **b)** energy comparison for $a/2 \langle 111 \rangle$ screw dislocation; **c)** energy comparison for $a \langle 100 \rangle$ screw dislocation

tive to that predicted by CGM) for the $a \langle 100 \rangle$ dislocations than the $a/2 \langle 111 \rangle$ dislocations at large defect densities. Furthermore, for $a/2 \langle 111 \rangle$ dislocations (Fig. 4(b)), a linear increase in stored defect energy with applied deformation F_{11} is observed. However, for $a \langle 100 \rangle$ dislocations (Fig. 4(c)), the defect energy remains virtually constant or decreases very slightly with applied deformation. For both classes of dislocations, an approximately linear in-

crease in E^d with increasing dislocation density α^{11} is evident. Also, comparing Figs. 4(b) and 4(c), for similar magnitudes of dislocation density, the defect energy for the $a \langle 100 \rangle$ dislocations is substantially greater, presumably due to a larger Burgers vector. For example, $E^d = 0.0184$ eV / atom for $a \langle 100 \rangle$ dislocations at $\alpha^{11} = 0.0035$/nm and at $F_{11} = 1.000$, while $E^d = 0.0114$ eV / atom for $a/2 \langle 111 \rangle$ dislocations at $\alpha^{11} = 0.0031$/nm and at $F_{11} = 1.000$.

5. CONTINUUM MODELING OF ENERGETICS OF POINT AND LINE DEFECTS

Considered next are continuum representations of energy density for W single crystals containing periodically distributed vacancies or screw dislocations. Note that no attempt is made to consider isolated dislocation energies, as has been the goal of previous studies [33]. Instead, the effects of neighboring defects are purposely included, thereby representing a distribution of lattice imperfections as would occur, for example, in a plastically deforming sample of material.

In the context of continuum defect field theories [66,87–89], one may decompose the tangent map from an initial, defect-free state $\bar{B}$ to the current configuration B multiplicatively, that is,

$$\mathbf{A} = \mathbf{FK} \quad A^a_{.\alpha} = F^a_{.A} K^A_{.\alpha} \quad (61)$$

where $\mathbf{F}$ is the compatible deformation gradient (Eq. (1)) from undeformed, but possibly defective, state B_0 to deformed configuration B; $\mathbf{K}$ represents insertion of defects into the macroscopically undeformed lattice; and $\mathbf{A}$ is the total deformation mapping. Greek indices denote components referred to basis vectors in defect-free configuration $\bar{B}$. The physics of Eq. (61) are illustrated conceptually in Fig. 5. Generally, neither $\mathbf{A}$ nor $\mathbf{K}$ is a compatible deformation mapping as defects such as dislocations and vacancies introduce discontinuities in the lattice, and there is no one-to-one correspondence between atoms in $\bar{B}$ and B_0. As such, skew-symmetric spatial gradients of anholonomic mappings $\mathbf{A}$ and $\mathbf{K}$ are generally nonvanishing [54,66].
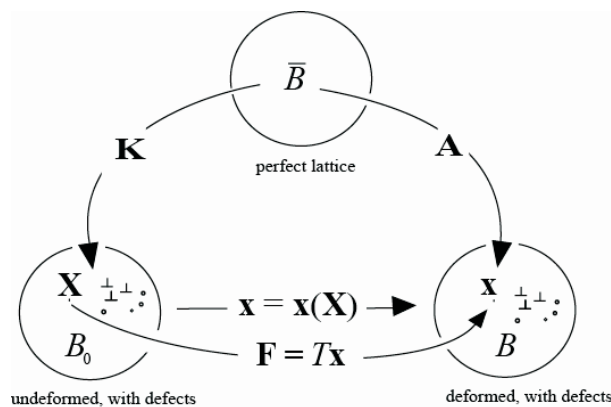

FIGURE 5. Configurations and tangent mappings in continuum defect theory

For a material with uniform and dilute vacancy density χ, contraction of the lattice attributed to vacancy formation is of the isotropic form [54,90]

$$K^A_{.\alpha} = (1 + \chi)^{-1/3} \delta^A_{.\alpha} \quad (62)$$

The corresponding strain energy density per atom, under isothermal conditions, can be written as

$$\Psi = \Psi_0 + (1 - \chi) \Psi_E + \chi \Psi_V \quad (63)$$

where Ψ_0 is the cohesive energy of the undeformed, defect-free lattice; Ψ_E is the recoverable elastic strain energy; and Ψ_V is the formation energy per vacancy. Note that Ψ in Eq. (63) may be converted to a per-unit-reference-volume basis via division by the atomic volume per atom β. To first order,

$$\begin{aligned} \Psi_E &= \tfrac{1}{2} \hat{\mathbb{C}}^{AB}_{ab} \left(F^a_{.A} - \delta^a_{.A} \right) \left(F^b_{.B} - \delta^b_{.B} \right) \\ &= \tfrac{1}{2} \mathbb{C}^{ABCD} E_{AB} E_{CD} \end{aligned} \quad (64)$$

where the elastic constants $\hat{\mathbb{C}}^{AB}_{ab}$ or $\mathbb{C}^{ABCD}$ are evaluated for a defect-free crystal at $F^a_{.A} = \delta^a_{.A}$ or $E_{AB} = 0$. Total energies relative to Ψ_0, computed via the CDF approach of Eq. (63), are compared quantitatively with those obtained from AEH calculations in Table 5 and Fig. 6. For W, the energetic parameters entering Eq. (63) are $\Psi_0 = E^C = -8.90$ eV / atom and $\Psi_V = 3.63$ eV. The elastic energy density Ψ_E used in the CDF approximation is determined here by subtracting Ψ_0 from the total energy of the deformed perfect lattice such that Eq. (64) is not used explicitly. As is clear from Table 5 and Fig. 6, for simulations 1–4, agreement between AEH and CDF is within 0.1% for the total energy $\Psi - \Psi_0$, even at the largest defect density of $\chi = 5.1 (10)^{-4}$. From Fig. 6, the total energy increases with the applied deformation in a quadratic fashion, with initial differences among the curves at $F_{11} = 1.000$ caused by differences in initial vacancy concentration, as accurately captured by the third term on the right-hand side of Eq. (63). Defect energy E^d is listed in Table 6. For the AEH method, this is computed via Eq. (59), while for the continuum defect theory, it is defined as summed magnitude of contributions of χ in Eq. (63) to elastic and initial energies:

$$E^d = \chi \left(\Psi_E + \Psi_V \right) \quad (65)$$

As is clear from Table 6, defect energies predicted by simulation and continuum approximation agree to within 1%, even at the highest vacancy concentration.

TABLE 5. Total energies described by multiscale theories: asymptotic expansion homogenization (AEH, computation) and continuum defect field (CDF, parameter fit)

Case #	Defect	Defect density	$\Psi - \Psi_0$[ev/atom], $F_{11} = 1.000$		$\Psi - \Psi_0$[ev/atom], $F_{11} = 1.025$	
			AEH	CDF	AEH	CDF
1	vacancy	$5.0(10)^{-4}$	$1.8021(10)^{-3}$	$1.8006(10)^{-3}$	0.016627	0.016604
2	vacancy	$1.2(10)^{-4}$	$4.5035(10)^{-4}$	$4.5015(10)^{-4}$	0.015263	0.015259
3	vacancy	$5.5(10)^{-5}$	$2.0014(10)^{-4}$	$2.0007(10)^{-4}$	0.015012	0.015001
4	vacancy	$3.1(10)^{-5}$	$1.1258(10)^{-4}$	$1.1254(10)^{-4}$	0.014924	0.014923
5	[111] disl.	0.0071/nm	0.021664	0.022616	0.040209	0.038572
6	[111] disl.	0.0031/nm	0.011379	0.010052	0.028345	0.025371
7	[111] disl.	0.0018/nm	$7.1017(10)^{-3}$	$5.6541(10)^{-3}$	0.023323	0.020751
8	[100] disl.	0.0316/nm	0.114262	0.150512	0.131972	0.169068
9	[100] disl.	0.0079/nm	0.036432	0.037628	0.054277	0.056184
10	[100] disl.	0.0035/nm	0.018391	0.016724	0.036445	0.035279
11	[100] disl.	0.0020/nm	0.011235	0.009407	0.029438	0.027963
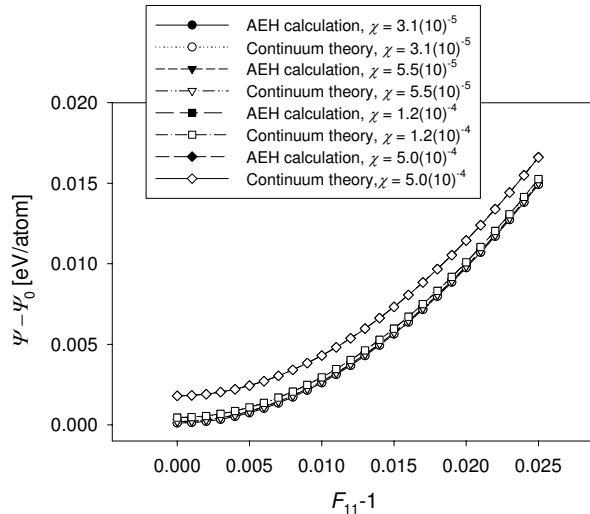
FIGURE 6. Computed (AEH) and continuum approximations (Eq. (63)) for total system energy of BCC tungsten with periodic vacancy density Ψ

In the continuum defect field theories, dislocations are considered to be continuously distributed, and the strain fields and displacement discontinuities of individual defects are not represented explicitly. Consider a crystal containing periodically spaced screw dislocations oriented along the X^1-axis. The deformation mapping attributed to such defects is of the form

$$\mathbf{K} = \delta^A_{.\alpha} \mathbf{G}_A \otimes \bar{\mathbf{g}}^\alpha + \gamma^1_{.2}\left(X^2, X^3\right) \mathbf{G}_1 \otimes \bar{\mathbf{g}}^2 + \gamma^1_{.3}\left(X^2, X^3\right) \mathbf{G}_1 \otimes \bar{\mathbf{g}}^3 \quad (66)$$

where the antiplane deformation components $\gamma^1_{.2}$ and $\gamma^1_{.3}$ are differentiable but generally nonintegrable functions of their arguments, and where $\mathbf{G}_A$ and $\bar{\mathbf{g}}^\alpha$ denote basis vectors on B_0 and $\bar{B}$, respectively. The density of GNDs may then be computed from gradients of $\mathbf{K}$ as follows [50,51,55,66,91]. The total Burgers vector $\mathbf{B}$ arising from all dislocations piercing area A can be expressed as the line or area integral

$$B^\alpha = -\oint_C K^{-1\alpha}_{.A} dX^A = \int_A \varepsilon^{ABC} K^{-1\alpha}_{.A,B} N_C dA \quad (67)$$

$$= \int_A K^{-1\alpha}_{.A} \bar{\alpha}^{AC} N_C dA = \int_A K^{-1\alpha}_{.A} \left(\sum_i \bar{\rho} b^A \xi^C\right) N_C dA$$

where C is a closed loop encircling A with unit normal $\mathbf{N}$ and α is the density of dislocations, defined in a discrete manner in Eq. (60) for one family of dislocations and generalized here as a summation over i families of dislocation segments each having constant Burgers vector $\mathbf{b}$ and tangent line ξ, both referred to reference configuration B_0. The permutation symbols are written ε^{ABC}. From Eq. (67) and the identity $\partial_{\mathbf{X}}\left(\mathbf{K}\mathbf{K}^{-1}\right) = 0$, the GND density tensor is then

$$\bar{\alpha}^{AC} = K^A_{.\alpha} \varepsilon^{DBC} K^{-1\alpha}_{.D,B} = -K^{-1\alpha}_{.D} \varepsilon^{DBC} K^A_{.\alpha,B} \quad (68)$$

The following general functional form of the isothermal free energy for a crystal with a nonzero dislocation density is postulated:

TABLE 6. Defect energies described by multiscale theories: asymptotic expansion homogenization (AEH, computation) and continuum defect field (CDF, parameter fit)

Case #	Defect	Defect density	E^d[ev/atom], $F_{11} = 1.000$		E^d[ev/atom], $F_{11} = 1.025$	
			AEH	CDF	AEH	CDF
1	vacancy	$5.0(10)^{-4}$	$1.8021(10)^{-3}$	$1.8006(10)^{-3}$	$1.8156(10)^{-3}$	$1.8079(10)^{-3}$
2	vacancy	$1.2(10)^{-4}$	$4.5035(10)^{-4}$	$4.5015(10)^{-4}$	$4.5252(10)^{-4}$	$4.5199(10)^{-4}$
3	vacancy	$5.5(10)^{-5}$	$2.0014(10)^{-4}$	$2.0007(10)^{-4}$	$2.0093(10)^{-4}$	$2.0088(10)^{-4}$
4	vacancy	$3.1(10)^{-5}$	$1.1258(10)^{-4}$	$1.1254(10)^{-4}$	$1.1299(10)^{-4}$	$1.1300(10)^{-4}$
5	[111] disl.	0.0071/nm	0.021664	0.022616	0.025399	0.023761
6	[111] disl.	0.0031/nm	0.011379	0.010052	0.013534	0.010561
7	[111] disl.	0.0018/nm	0.007102	0.005654	0.008513	0.005940
8	[100] disl.	0.0316/nm	0.114262	0.150512	0.113417	0.150512
9	[100] disl.	0.0079/nm	0.036432	0.037628	0.035721	0.037628
10	[100] disl.	0.0035/nm	0.018391	0.016724	0.017889	0.016724
11	[100] disl.	0.0020/nm	0.011235	0.009407	0.010882	0.009407

$$\Psi = \Psi_0 + \Psi_E + \mu \left(l^2 \alpha^{AB} \hat{G}_{AC} \hat{G}_{BD} \alpha^{CD} \right)^m \quad (69)$$

where $\hat{\mathbf{G}}$ is a (dimensionless) metric tensor defined on B_0 used to compute the inner product of the contravariant tensor $\boldsymbol{\alpha}$, μ is an elastic shear modulus (constant), and l (units of length) and m (dimensionless) are scalars. For W of interest here, $\mu = 159$ GPa $= 16.07$ eV / atom. Typically, the metric in Eq. (69) is selected for simplicity as $\hat{G}_{AB} = \delta_{AB}$ [51–53]; however, there is some evidence that other choices may be more appropriate. Gibeling and Nix [92] discussed, from the standpoint of discrete dislocation modeling, how the strain energy sustained by dislocations may be amplified by externally applied deformations. As such, following [66,93], the covariant elastic deformation measure $\hat{G}_{AB} = C_{AB} = F^a_{.A} g_{ab} F^b_{.B}$ may be used in Eq. (69) to reflect amplification of internal defect energy commensurate with applied deformation. The choice of m in Eq. (69) also warrants careful consideration. Most often in recent literature, $m = 1$ is used to reflect a quadratic dependence of the free energy on the GND tensor [51–53]. This form is often invoked, in conjunction with thermodynamic arguments, to provide a back stress dependent on the density tensor of dislocations [52,64] and/or its spatial gradient [51,53]. Clayton [63] assumed a linear dependence ($m = 1/2$) of stored energy on dislocation density in a continuum crystal plasticity model of single crystalline W. A linear dependence of free energy on SSD density is also commonly prescribed [52]. Fi-

nally, in continuum dislocation–based plasticity theories, the length parameter l is often calibrated in a phenomenological manner to reflect the degree of additional stiffness or strain hardening imparted by the dislocation density, for example, in torsion of a thin wire [94] or in nanoindentation [95,96].

In the present work, parameters l and m entering Eq. (69) are computed directly via a best fit to results from AEH calculations, as opposed to a calibration to macroscopic data. For both $a/2 \langle 111 \rangle$ and $a \langle 100 \rangle$ dislocations, $m = 1/2$ provides a superior fit to the computational results than does $m = 1$. Since the defect energy E^d in Fig. 4(b) for $a/2 \langle 111 \rangle$ dislocations increases with applied deformation, $\hat{G}_{AB} = C_{AB} = F^a_{.A} g_{ab} F^b_{.B}$ is used for dislocations of that orientation. Note that for uniaxial strain of the form $F_{11} = 1 + \bar{\varepsilon}$, with screw dislocations oriented parallel to the X^1-direction, the defect energy in Eq. (69) degenerates to

$$E^d = \mu \left(l^2 \alpha^{AB} \hat{G}_{AC} \hat{G}_{BD} \alpha^{CD} \right)^{1/2}$$
$$= \mu l \alpha^{11} \left(1 + 2\bar{\varepsilon} + \bar{\varepsilon}^2 \right) \quad (70)$$

On the other hand, since the energy E^d in Fig. 4(c) of $a \langle 100 \rangle$ dislocations remains relatively constant with applied loading, $\hat{G}_{AB} = \delta_{AB}$ is used for representing the energy of $a \langle 100 \rangle$ dislocations, meaning that Eq. (69) applies in that case with $\bar{\varepsilon} = 0$. For $a/2 \langle 111 \rangle$ dislocations, $l = 0.200$ nm $= 0.73b$, and for $a \langle 100 \rangle$ dislocations, $l = 0.297$ nm $= 0.94b$. These values are much smaller in magnitude than

some of those calibrated from macroscopic data, with l reported in the latter on the order of several micrometers [94,95], though values in the nanometer range have been suggested for l from hardness measurements inferred from indentation data [96]. Comparisons of the energy $\Psi - \Psi_0$ described by the CDF theory of Eq. (69) with numerical predictions from AEH over the range of uniaxial deformation $1.000 \leq F_{11} \leq 1.025$ are shown in Fig. 7 for $a/2 \langle 111 \rangle$ dislocations and in Fig. 8 for $a \langle 100 \rangle$ dislocations. For ease of quantitative comparison, values at $F_{11} = 1.000$ and $F_{11} = 1.025$ are tabulated for the relative total energy $\Psi - \Psi_0$ in Table 5 and defect energy E^d in Table 6. The agreement between AEH and CDF predictions is generally modest and is closest at relatively large defect densities, that is, for $\alpha^{11} > 0.005$ / nm.

The investigation conducted here is limited in the sense that only a few classes of screw dislocations are examined, for only one material, and these defects are arranged periodically in the lattice. Furthermore, all simulations are isothermal at null temperature (akin to molecular statics). However, the work represents an initial step toward computing energies used in continuum defect theories from physics-based, multiscale-atomistic computations, as opposed to phenomenological curve fit-
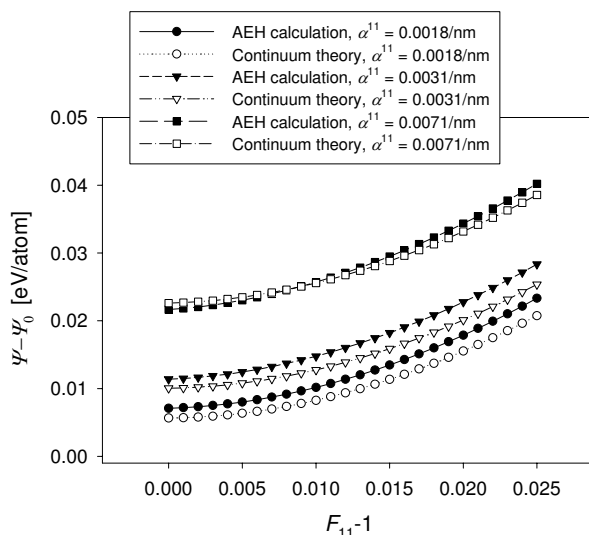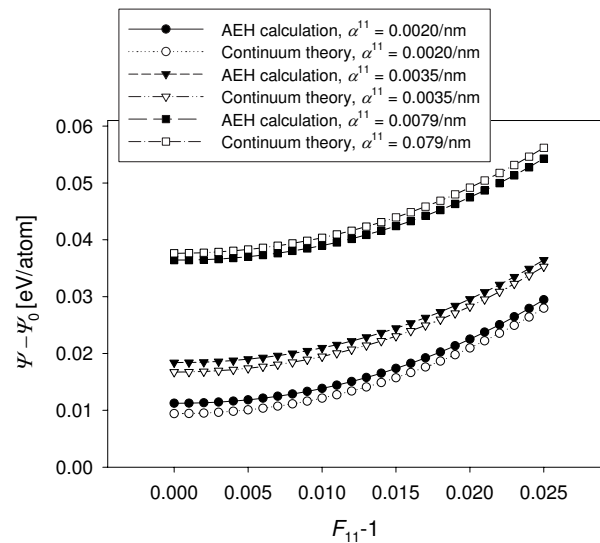

FIGURE 8. Computed (AEH) and continuum approximations (Eq. (69)) of energy for BCC tungsten with nonzero dislocation density component α^{11} arising from periodic $a \langle 100 \rangle$ screw dislocations

FIGURE 7. Computed (AEH) and continuum approximations (Eq. (69)) of energy for BCC tungsten with nonzero dislocation density component α^{11} arising from periodic $a/2 \langle 111 \rangle$ screw dislocations

ting to macroscopic stress-strain or microindentation data, for example. The dislocation densities considered here, with $\bar{\rho}$ on the order of $10^{16}/\text{m}^2$, are quite large relative to densities found in homogeneously deforming single crystals. Argon and Maloof [97] reported values of $\bar{\rho}$ on the order of $10^{12}/\text{m}^2$ for pure tungsten single crystals deformed up to 5% axial tensile strain. Densities examined presently correspond to a dislocation spacing on the order of 10 nm. In highly strained regions of crystal, such as in the vicinity of grain or subgrain boundaries formed during severe plastic deformation (SPD), such tight spacing may not be unreasonable. For example, if one considers a boundary comprising a sequence of dislocations of spacing h and Burgers vector $\mathbf{b}$, the misorientation at the boundary can be computed as $\mathbf{b}/h$ [98], on the order of 4° for 10-nm-spaced dislocations in tungsten. For subgrain boundaries produced in tungsten crystals deformed through SPD processes [99,100], misorientations of such magnitude have been documented. Furthermore, strain gradient–based continuum defect theories are designed to address such phenomena in the context of crystal plasticity [51–55], so results presented here may be applied to motivate continuum energy dependencies, at least in a qualitative sense, on defect densities that serve

an important role in such theories. The thermodynamics of stored energy of cold working may also influence shear localization processes in ultra fine grained tungsten [100,101], a material that can exhibit dislocation densities of the magnitudes studied here.

6. CONCLUSIONS

A multiscale method based on the theory of asymptotic expansion homogenization is developed and implemented. The technique enables computation of global or coarse-grained mechanical properties such as effective elastic stiffness and net stress of a deforming unit cell consisting of periodically arranged, discrete atoms at the fine scale. The formulation directly accounts for the effects of defects in the lattice. From a computational standpoint, the method is an efficient alternative to incremental conjugate gradient schemes in terms of prediction of minimum energy configurations of atomic degrees of freedom in statically deforming lattices containing defects. The direction of a perturbative displacement—which serves as a correction to the CB rule which is accurate only for homogeneous deformations—is computed via application of the homogenization scheme in an equation that relates the free energy of the system, the macroscopic deformation gradient, and local atomic degrees of freedom. The key computational advantage of this approach, relative to traditional molecular statics or molecular dynamics, is the use of a directed line search algorithm, which reduces the energy minimization process from minimization over traditional $3 \times \mathbb{N}$ solution space to a line search in one dimension (with this direction determined as mentioned above via solution of the fine-scale equilibrium equation of the homogenization scheme). The current multiscale method also does not present any difficulties associated with matching boundary conditions across length scales since the displacement gradient, rather than displacements themselves, is the kinematic quantity exchanged between scales. In validation simulations with predefined defect structures, close agreement is found with energies predicted by the present method and conjugate gradient-based molecular mechanics, and categorically lower system energies are predicted than those obtained from the CB rule.

Specifically studied here are the nonlinear elastic responses of BCC tungsten single crystals containing periodically distributed vacancies and screw dislocations of two different classes. It is found that energies associated with vacancies and $a/2 \langle 111 \rangle$ screw dislocations tend to increase with applied uniaxial stretching, while energies of $a \langle 100 \rangle$ screw dislocations tend to remain constant with stretch. These computed energies are used to motivate continuum energy functions for defective crystals described in terms of the vacancy density, the dislocation density tensor, and/or the applied deformation gradient. For crystals with vacancies, a continuum description of defect energy increasing linearly with vacancy density is found to be extremely accurate, relative to the computational results, over the range of defect densities considered. For W with screw dislocations, a defect energy linearly dependent on dislocation density provides better agreement with numerical results than does a quadratic dependency of this energy on the dislocation density tensor often encountered in dislocation-based gradient plasticity theory.

The method and results presented here offer several avenues for improvement of existing crystal elasticity and plasticity models. The present focus has been on the nonlinear elastic response as well as construction of elastic strain- and defect-energy functions entering continuum gradient plasticity theories. The results could be used in stand-alone crystal plasticity theory, either classical local theory [102] or nonlocal gradient theory [55], in either case with the stored energy and elastic moduli allotted an explicit dependence on initial defect content. More ambitiously, the present homogenization technique could be incorporated in a discrete-continuum multiscale context, with elastic modulus and stored energy depending on the fine-scale configuration of defects resolved concurrently in the simulation; such an idea was pursued in [45] for single slip conditions. Finite temperature effects would be needed for realistic resolution of dislocation dynamics. Incorporation of such effects would involve some reformulation of the governing equations to account for dynamic as opposed to static conditions, beginning with Eq. (4), or consideration of alternative computational strategies for irreversible thermodynamics, as discussed below. In principle, thermally activated dislocation line motion could then be transferred upward in scale to describe continuum plastic deformation [50].

Finally, it is appropriate to note the scope of potential applications and some of the limitations of the method proposed in this article. Consider specifically the developments leading to Eq. (32) and several of the general underlying assumptions of the homogenization technique. The use of a truncated expansion of the strain energy presumes that the system stays in the positive definite region of the energy landscape and that the deformations considered are primarily of the thermodynamically reversible kind. While it is possible to incorporate irreversible mechanisms, as has been attempted in [45] by prescribing specific kinetic pathways for dislocation glide, the development of general models accounting for irreversible continuum-scale mechanisms such as, say, plasticity, based on atomistic interactions, has yet to be fully realized. Such models would be needed to account for dissipation and the nonequilibrium effects associated with energy transfer in and around the simulation domain. In such cases, modeling approaches using a generalized homogenization method to account for the time variable may be needed [46].

The limitations imposed on possible applications by the assumption of periodicity merit reiteration. In this work, the primary results stem from the accounting of the physically inhomogeneous deformation around crystal defects, with a demonstrated connection between atomic and continuum modeling methods. Insofar as the distribution of imperfections such as dislocations can be described as being periodic, the proposed homogenization method is applicable [33], with suitable accuracy, as suggested by the results reported here. In the event that the system departs from periodicity, a common occurrence in the irreversible regime, where dislocations move and can ultimately pile up along interfaces, adaptive modeling approaches [103–106] may be most suitable. In such instances, heterogeneous solution domains involving some subdomains modeled through homogenization, as described here, and others modeled with quasicontinuum theory [26–28] or direct molecular statics, for example, would be appropriate. Investigations of the like suggest interesting directions for future work. With the present homogenization technique, it should also be noted that periodicity of the lattice enables one to consider a reduced number of atoms, relative to a more disordered material, at the fine scale. For example, modeling of a single crystal of uniform lattice orientation generally requires far fewer atoms than would realistically modeling a polycrystal. The latter, though conceptually feasible, would require computationally costly atomistic resolution of grain boundaries and intergranular misorientations.

ACKNOWLEDGMENTS

REFERENCES

1. Cauchy, A.-L., Sur l'equilibre et le movement d'un systeme de points materiels sollicites par forces d'attraction ou de repulsion mutuelle. *Exer. Math.* **3**:227–287, 1828.

2. Born, M., and Huang, K., *Dynamical Theory of Crystal Lattices*. Clarendon Press, Oxford, 1988.

3. Ericksen, J. L., *Phase Transformations and Material Instabilities in Solid*s. Academic Press, New York, 1984.

4. Zanzotto, G., On the material symmetry group of elastic crystals and the Born rule. *Arch. Ration. Mech. Anal.* **121**:1–36, 1992.

5. Zanzotto, G., Nonlinear elasticity, the Cauchy-Born hypothesis, and mechanical twinning in crystals. *Acta Cryst. A.* **52**:839–849, 1996.

6. Arroyo, M., and Belytschko, T., An atomistic-based finite deformation membrane for single layer crystalline films. *J. Mech. Phys. Solids.* **50**:1941–1947, 2002.

7. Sunyk, R., and Steinmann, P., On higher gradients in continuum-atomistic modeling. *Int. J. Solids Struct.* **40**:6877–6896, 2003.

8. Leamy, M. J., Chung, P. W., and Namburu, R. R., On an exact mapping and higher order born rule for use in analyzing graphene carbon nanotubes. Tech. Rep. A413914. U.S. Army Research Laboratory, Aberdeen Proving Ground, MD, 2003.

9. Gehlen, P. C., Rosenfield, A. R., and Hahn, G. T., Structure of the $\langle 100 \rangle$ edge dislocation in iron. *J. Appl. Phys.* **39**:5246–5254, 1968.

10. Chang, R., An atomistic study of fracture. *Int. J. Fract. Mech.* **6**:111–125, 1970.

11. Sinclair, J. E., and Lawn, B. R., Atomistic study of cracks in diamond-structure crystals. *Proc. R. Soc. London, Ser. A.* **329**:83–103, 1972.

12. Weiner, J. H., and Pear, M., Crack and dislocation propagation in an idealized crystal model. *J. Appl. Phys.* **46**:2398–2405, 1975.

13. DeCelis, B., Argon, A. S., and Yip, S., Molecular dynamics simulation of crack tip processes in alpha-iron and copper. *J. Appl. Phys.* **54**:4864–4878, 1983.

14. Cheung, K. S., and Yip, S., Brittle-ductile transition in intrinsic fracture behavior of crystals. *Phys. Rev. Lett.* **65**:2804–2807, 1990.

15. Johnson, R. A., Interstitials and vacancies in α-iron. *Phys. Rev.* **134**:1329–1336, 1964.

16. Gehlen, P. C., Hahn, G. T., and Kanninen, M. F., Crack extension by bond rupture in a model of bcc iron. *Scr. Metall.* **6**:1087–1090, 1972.

17. Sinclair, J. E., Gehlen, P. C., Hoagland, R. G., and Hirth, J. P., Flexible boundary conditions and nonlinear geometric effects in atomistic dislocation modeling. *J. Appl. Phys.* **49**:3890–3897, 1978.

18. Zhou, S. J., Carlsson, A. E., and Thomson, R., Dislocation nucleation and crack stability: Lattice Green's function treatment of cracks in a model hexagonal lattice. *Phys. Rev. B.* **47**:7710–7719, 1993.

19. Noguchi, H., and Furuya, Y., A method of seamlessly combining a crack tip molecular dynamics enclave with a linear-elastic outer domain in simulation of elastic-plastic crack advance. *Int. J. Fract.* **87**:309–329, 1997.

20. Mullins, M., Molecular dynamics simulation of propagating cracks. *Scr. Metall.* **16**:663–666, 1982.

21. Mullins, M., Computer simulation of fracture using long range pair potentials. *Acta Metall.* **32**:381–388, 1984.

22. Mullins, M., and Dokainish, M. A., Simulation of the (001) plane crack in α-iron employing a new boundary scheme. *Philos. Mag. A.* **46**:771–787, 1982.

23. Kohlhoff, S., Gumbsch, P., and Fischmeister, H. F., Crack propagation in b.c.c. crystals studied with a combined finite-element atomistic model. *Philos. Mag. A.* **64**:851–878, 1991.

24. Abraham, F. F., Broughton, J. Q., Bernstein, N., and Kaxiras, E., Spanning the continuum to quantum length scales in a dynamic simulation of brittle fracture. *Europhys. Lett.* **44**:783–787, 1998.

25. Broughton, J. Q., Abraham, F. F., Bernstein, N., and Kaxiras, E., Concurrent coupling of length scales: Methodology and application. *Phys. Rev. B.* **60**:2391–2403, 1999.

26. Tadmor, E. B., Ortiz, M., and Phillips, R., Quasicontinuum analysis of defects in solids. *Philos. Mag. A .***73**:1529–1563, 1996.

27. Miller, R., Tadmor, E. B., Ortiz, M., and Phillips, R., Quasicontinuum simulation of fracture at the atomic scale. *Model. Simul. Mater. Sci. Eng.* **6**:607–638, 1998.

28. Shenoy, V. B., Miller, R., Tadmor, E., Philips, R., and Ortiz, M., Quasicontinuum models of interfacial structure and deformation. *Phys. Rev. Lett.* **80**:742–745, 1998.

29. Cleri, F., Phillpot, S. R., Wolf, D., and Yip, S., Atomistic simulation of materials fracture and the link between atomic and continuum length scales. *J. Am. Ceram. Soc.* **81**:501–516, 1998.

30. Curtin, W. A., and Miller, R. E., Atomistic/continuum coupling in computational materials science. *Model. Simul. Mater. Sci. Eng.* **11**:R33–R68, 2003.

31. Liu, W. K., Karpov, E. G., Zhang, S., and Park, H. S., An introduction to computational nanomechanics and materials. *Comput. Methods Appl. Mech. Eng.* **193**:1529–1578, 2004.

32. Fago, M., Hayes, R. L., Carter, E. A., and Ortiz, M., Density functional theory based local quasicontinuum method: Prediction of dislocation nucleation. *Phys. Rev. B.* **70**:100–102, 2004.

33. Cai, W., Bulatob, V. V., Chang, J., Li, J., and Yip, S., Periodic image effects in dislocation modeling. *Philos. Mag.* **83**:539–567, 2003.

34. Kowalewsky, O., Theory of complex lattice quasicontinuum and its application to ferroelectrics. PhD thesis, California Institute of Technology, Pasadena, 2004.

35. Tewary, V. K., Green's function method for lattice statics. *Adv. Phys.* **22**:757–810, 1973.

36. Thomson, R., Zhou, S. J., Carlsson, A. E., and Tewary, V. K., Lattice imperfections studied by

use of lattice Green's functions. *Phys. Rev. B.* **46**:10613–10622, 1993.

37. Rudd, R. E., and Broughton, J. Q., Coarse-grained molecular dynamics and the atomic limit of finite elements. *Phys. Rev. B.* **58**:5893–5896, 1998.

38. Cai, W., De Koning, M., Bulatov, V. V., and Yip, S., Minimizing boundary reflections in coupled-domain simulations. *Phys. Rev. Lett.* **85**:3213–3216, 2000.

39. E, W., and Huang, Z. Y., Matching conditions in atomistic-continuum modeling of materials. *Phys. Rev. Lett.* **87**:135501, 2001.

40. Park, H. S., Karpov, E. G., and Liu, W. K., A temperature equation for coupled atomistic/continuum simulations. *Comput. Methods Appl. Mech. Eng.* **60**:833–859, 2004.

41. Chung, P. W., and Namburu, R. R., On a formulation for a multiscale atomistic-continuum homogenization method. *Int. J. Solids Struct.* **40**:2563–2588, 2003.

42. Chung, P. W., Computational method for atomistic homogenization of nanopatterned point defect structures. *Int. J. Numer. Methods Eng.* **60**:833–859, 2004.

43. Bensoussan, A., Lions, J. L., and Papanicolaou, G., *Asymptotic Analysis for Periodic Structures*. North Holland, Amsterdam, Netherlands, 1978.

44. Sanchez-Palencia, E., *Non-homogeneous Media and Vibration Theory*. Lecture Notes in Physics, vol. 127. Springer, Berlin, 1980.

45. Clayton, J. D., and Chung, P. W., An atomistic framework for nonlinear crystal mechanics based on asymptotic homogenization. *J. Mech. Phys. Solids.* **54**:1604–1639, 2006.

46. Chen, W., and Fish, J., A generalized space-time mathematical homogenization theory for bridging atomistic and continuum scales. *Int. J. Numer. Methods Eng.* **67**:253–271, 2006.

47. Fish, J., Chen, W., and Li, R., Generalized mathematical homogenization of atomistic media at finite temperatures in three dimensions. *Comput. Methods Appl. Mech. Eng.* **196**:908–922, 2007.

48. Papadrakakis, M., and Ghionis, P., Conjugate-gradient algorithms in nonlinear structural-analysis problems. *Comput. Methods Appl. Mech.*

Eng. **59**:11–27, 1986.

49. Plimpton, S. J., and Hendrickson, B. A., Parallel molecular dynamics with the embedded atom method. In *Materials Theory and Modelling*. MRS Proceedings, vol. 291. Broughton, J., Bristowe, P., and Newsam, J., Eds., Materials Research Society, Pittsburgh, PA, 37–42, 1993.

50. Teodosiu, C., A dynamic theory of dislocations and its application to the theory of elastic-plastic continuum. In *Fundamental Aspects of Dislocation Theory*. NBS Special Publication, vol. 317. U.S. Government Printing Office, Gaithersburg, MD, 837–876, 1970.

51. Steinmann, P., Views on multiplicative elastoplasticity and the continuum theory of dislocations. *Int. J. Eng. Sci.* **34**:1717–1735, 1996.

52. Bammann, D. J., A model of crystal plasticity containing a natural length scale. *Mater. Sci. Eng. A.* **309–310**:406–410, 2001.

53. Gurtin, M. E., A gradient theory of single-crystal viscoplasticity that accounts for geometrically necessary dislocations. *J. Mech. Phys. Solids.* **50**:5–32, 2002.

54. Clayton, J. D., Bammann, D. J., and McDowell, D. L., A geometric framework for the kinematics of crystals with defects. *Philos. Mag.* **85**:3983–4010, 2005.

55. Clayton, J. D., McDowell, D. L., and Bammann, D. J., Modeling dislocations and disclinations with finite micropolar elastoplasticity. *Int. J. Plasticity.* **22**:210–256, 2006.

56. Menzel, A., and Steinmann, P., On the continuum formulation of higher gradient plasticity for single and polycrystals. *J. Mech. Phys. Solids.* **48**:1777–1796, 2000.

57. Abu Al-Rub, R. K., and Voyiadjis, G. Z., A finite strain plastic-damage model for high velocity impact using combined viscosity and gradient localization limiters: Part I—Theoretical formulation. *Int. J. Damage Mech.* **15**:293–334, 2006.

58. Milstein, F., and Chantasiriwan, S,. Theoretical study of the response of 12 cubic metals to uniaxial loading. *Phys. Rev. B.* **58**:6006–6018, 1998.

59. Milstein, F., Zhao, J., and Maroudas, D., Atomic pattern formation at the onset of stress-induced elastic instability: Fracture versus phase change. *Phys. Rev. B.* **70**:184102, 2004.

60. Bammann, D. J., Chiesa, M. L., Horstemeyer, M. F., and Weingarten, L. I., Failure in ductile materials using finite element methods. In *Structural Crashworthiness and Failure*. Jones, N. and Wierzbicki, T., Eds. Elsevier Applied Science, London, 1–53, 1993.

61. Chaboche, J. L., Continuum damage mechanics. 1. General concepts. *ASME J. Appl. Mech.* **55**:59–64, 1988.

62. Ashby, M. F., The deformation of plastically non-homogeneous materials. *Philos. Mag.* **21**:399–424, 1970.

63. Clayton, J. D., Dynamic plasticity and fracture in high density polycrystals: Constitutive modeling and numerical simulation. *J. Mech. Phys. Solids.* **53**:261–301, 2005.

64. Taylor, G. I., The mechanism of plastic deformation of crystals. *Proc. R. Soc. London, Ser. A.* **145**:362–415, 1934.

65. Voyiadjis, G. Z., and Abu Al-Rub, R. K., Gradient plasticity with a variable length scale parameter. *Int. J. Solids Struct.* **42**:3998–4029, 2005.

66. Clayton, J. D., Bammann, D. J., and McDowell, D. L., Anholonomic spaces and metric tensors in finite elastoplasticity. *Int. J. Nonlinear Mech.* **39**:1039–1049, 2004.

67. Zhou, M., A new look at the atomic level virial stress: On continuum-molecular system equivalence. *Proc. R. Soc. London, Ser. A.* **459**:2347–2392, 2003.

68. Koslowski, M., Cuitino, A. M., and Ortiz, M., A phase-field theory of dislocation dynamics, strain hardening, and hysteresis in ductile single crystals. *J. Mech. Phys. Solids.* **50**:2597–2635, 2002.

69. Berry, J., Grant, M., and Elder, K. R., Diffusive atomistic dynamics of edge dislocations in two dimensions. *Phys. Rev. E.* **73**:031609, 2006.

70. Groma, I., and Pawley, G. S., Computer simulation of plastic behaviour of single crystals. *Philos. Mag. A.* **67**:1459–1470, 1993.

71. Deshpande, V. S., Needleman, A., and Van der Giessen, E., Finite strain discrete dislocation plasticity. *J. Mech. Phys. Solids.* **51**:2057–2083, 2003.

72. Zbib, H. M., Shehadeh, M., Khan, S. M. A., and Karami, G., Multiscale dislocation dynamics plasticity. *Int. J. Multiscale Comput. Eng.* **1**:73–90, 2003.

73. Fish, J., and Chen, W., Discrete-to-continuum bridging based on multigrid principles. *Comput. Methods Appl. Mech. Eng.* **193**:1693–1711, 2004.

74. Vitek, V., Computer simulation of the screw dislocation motion in b.c.c. metals under the effect of the external shear and uniaxial stresses. *Proc. R. Soc. London, Ser. A.* **352**:109–124, 1976.

75. Zhou, M., and Clifton, R. J., Dynamic constitutive and failure behavior of a two-phase tungsten composite. *ASME J. Appl. Mech.* **64**:487–494, 1997.

76. Finnis, M. W., and Sinclair, J. E., A simple empirical N-body potential for transition metals. *Philos. Mag. A.* **50**:45–55, 1984.

77. Ackland, G. J., and Thetford, R., An improved N-body semi-empirical model for body-centered cubic transition metals. *Philos. Mag. A.* **56**:15–30, 1987.

78. Duesberry, M. S., and Vitek, V., Plastic anisotropy in B.C.C. transition metals. *Acta Mater.* **46**:1481–1492, 1998.

79. Liu, X., Golubov, S. I., Woo, C. H., and Huang, H., Glide of edge dislocations in tungsten and molybdenum. *Mater. Sci. Eng. A.* **365**:96–100, 2004.

80. Tian, X., and Woo, C., The movement of screw dislocations in tungsten. *Mater. Sci. Eng. A.* **369**:210–214, 2004.

81. Dupuy, L. M., Tadmor, E. B., Miller, R. E., and Phillips, R., Finite-temperature quasicontinuum: Molecular dynamics without all the atoms. *Phys. Rev. Lett.* **85**:060202, 2005.

82. Schultz, H., Defect parameters of b.c.c. metals: Group-specific trends. *Mater. Sci. Eng. A.* **141**:149–167, 1991.

83. Vitek, V., Theory of the core structures of dislocations in body-centered-cubic metals. *Cryst. Lattice Defects.* **5**:1–34, 1974.

84. Hirth, J. P., and Lothe, J., *Theory of Dislocations.* 2nd ed. Krieger, Malabar, FL, 1982.

85. Nye, J. F., Some geometrical relations in dislocated crystals. *Acta Metall.* **1**:153–162, 1953.

86. Groger, R., DDPLOT v. 2.3. Department of Ma-

terials Science and Engineering, University of Pennsylvania, Philadelphia, 2004.

87. Bilby, B. A., Bullough, R., and Smith, E., Continuous distributions of dislocations: A new application of the methods of non-Riemannian geometry. *Proc. R. Soc. London, Ser. A.* **231**:263–273, 1955.

88. Noll, W., Materially simple bodies with inhomogeneities. *Arch. Ration. Mech. Anal.* **27**:1–32, 1967.

89. Hartley, C. S., A method for linking thermally activated dislocation mechanisms of yielding with continuum plasticity theory. *Philos. Mag.* **83**:3783–3808, 2003.

90. Kroner, E., The differential geometry of elementary point and line defects in Bravais crystals. *Int. J. Theor. Phys.* **29**:1219–1237, 1990.

91. Lardner, R. W., *Mathematical Theory of Dislocations and Fracture*. University of Toronto Press, Canada, 1974.

92. Gibeling, J. C., and Nix, W. D., A numerical study of long range internal stresses associated with subgrain boundaries. *Acta Metall.* **28**:1743–1752, 1980.

93. Maugin, G. A., Material forces: Concepts and applications. *Appl. Mech. Rev.* **48**:213–245, 1995.

94. Fleck, N. A., Muller, G. M., Ashby, M. F., and Hutchinson, J. W., Strain gradient plasticity: Theory and experiment. *Acta Metall. Mater.* **42**:475–487, 1994.

95. Nix, W. D., and Gao, H. J., Indentation size effects in crystalline materials: A law for strain gradient plasticity. *J. Mech. Phys. Solids.* **46**:411–425, 1998.

96. Abu Al-Rub, R. K., and Voyiadjis, G. Z., Analytical and experimental determination of the material intrinsic length scale of strain gradient plasticity theory from micro- and nano-indentation experiments. *Int. J. Plasticity.* **20**:1139–1182, 2004.

97. Argon, A., and Maloof, S. R., Plastic deforma-

tion of tungsten crystals at low temperatures. *Acta Metall.* **14**:1449–1462, 1966.

98. Hughes, D. A., Hansen, N., and Bammann, D. J., Geometrically necessary boundaries, incidental dislocation boundaries, and geometrically necessary dislocations. *Scr. Mater.* **48**:147–153, 2003.

99. Valiev, R. Z., Islamgaliev, R. K., and Tumentsev, A. N., The disclination approach for nanostructured SPD materials. *Solid State Phenom.* **87**:255–264, 2002.

100. Wei, Q., Jiao, T., Ramesh, K. T., Ma, E., Kecskes, L. J., Magness, L., Dowding, R., Kazykhanov, V. U., and Valiev, R. Z., Mechanical behavior and dynamic failure of high-strength ultrafine grain tungsten under uniaxial compression. *Acta Mater.* **54**:77–87, 2006.

101. Wei, Q., Ramesh, K. T., Ma, E., Kesckes, L. J., Dowding, R. J., Kazykhanov, V. U., and Valiev, R. Z., Plastic flow localization in bulk tungsten with ultrafine microstructure. *Appl. Phys. Lett.* **86**:101907, 2005.

102. Asaro, R. J., Crystal plasticity. *ASME J. Appl. Mech.* **50**:921–934, 1983.

103. Oden, J. T., and Zohdi, T. I., Analysis and adaptive modeling of highly heterogeneous elastic structures. *Comput. Methods Appl. Mech. Eng.* **148**:367–391, 1997.

104. Vemaganti, K., and Oden, J. T., Estimation of local modeling error and goal-oriented adaptive modeling of heterogeneous materials, Part II: A computational environment for adaptive modeling of heterogeneous elastic solids. *Comput. Methods Appl. Mech. Eng.* **190**:6029–6214, 2001.

105. Raghavan, P., and Ghosh, S., Adaptive multiscale modeling of composite materials. *Comput. Model. Eng. Sci.* **5**:151–170, 2004.

106. Ghosh, S., Bai, J., and Raghavan, P., Concurrent multi-level model for damage evolution in microstructurally debonding composites. *Mech. Mater.* **39**:241–266, 2007.

NO. OF
COPIES ORGANIZATION

1   DEFENSE TECHNICAL
(PDF   INFORMATION CTR
ONLY)   DTIC OCA
        8725 JOHN J KINGMAN RD
        STE 0944
        FORT BELVOIR VA 22060-6218

1   US ARMY RSRCH DEV &
        ENGRG CMD
        SYSTEMS OF SYSTEMS
        INTEGRATION
        AMSRD SS T
        6000 6TH ST STE 100
        FORT BELVOIR VA 22060-5608

1   DIRECTOR
        US ARMY RESEARCH LAB
        IMNE ALC IMS
        2800 POWDER MILL RD
        ADELPHI MD 20783-1197

1   DIRECTOR
        US ARMY RESEARCH LAB
        AMSRD ARL CI OK TL
        2800 POWDER MILL RD
        ADELPHI MD 20783-1197

1   DIRECTOR
        US ARMY RESEARCH LAB
        AMSRD ARL CI OK T
        2800 POWDER MILL RD
        ADELPHI MD 20783-1197

        ABERDEEN PROVING GROUND

1   DIR USARL
        AMSRD ARL CI OK TP (BLDG 4600)

NO. OF
COPIES ORGANIZATION

ABERDEEN PROVING GROUND

20   DIR USARL
      AMSRD ARL WM TD
        J CLAYTON (10 CPS)
      AMSRD ARL CI HC
        P CHUNG (10 CPS)